Straining and Scalar Dissipation on Material Surfaces in Turbulence: Implications for Flamelets

P. K. YEUNG,* S. S. GIRIMAJI and S. B. POPE

Sibley School of Mechanical and Aerospace Engineering, Cornell University, Ithaca, NY 14853

Direct numerical simulations of turbulence are used to examine the straining on material surfaces, and the behavior of thin diffusive layers. The results are related to questions arising in the study of turbulent premixed and diffusion flames in the flamelet regime. The simulations are of constant-density, homogeneous, isotropic turbulence, with artificial forcing of the velocity field to maintain statistical stationarity. Taylor-scale Reynolds numbers (R_λ) up to 93 are achieved.

It is found that the total rate-of-strain a in the tangent plane of a material surface is positive (i.e., extensive) with 80% probability. This straining causes the area of the surface to double every 2.5 Kolmogorov time scales (τ_η). A premixed flamelet can be viewed as a surface that propagates at a speed w (i.e., the local laminar flame speed) relative to the fluid ahead. It is shown that the distance z between such a propagating surface and an initially coincident material surface remains small if w is small compared to the Kolmogorov velocity scale. For this case, the statistics of z are characterized.

Subject to certain assumptions, the thin diffusive layers between blobs of fluid of different concentration adopt a self-similar form (at least for small times). It is found that the scalar dissipation χ_0 in the center of these layers is approximately log-normally distributed. The mean thickness of these layers is approximately 2 Batchelor scales, and is less than 5 Batchelor scales with 98% probability. The joint probability density of χ_0 and a shows that χ_0 fluctuates significantly about its quasi-static value based on a (for $a > 0$). The integral time scales of a and χ_0 are found to be approximately τ_η and $4\tau_\eta$, respectively. None of the results obtained shows significant Reynolds-number dependence when normalized by the Kolmogorov scales.

1. INTRODUCTION

Flamelet approaches, reviewed by Peters [1], have been used as the bases for models of both premixed and nonpremixed turbulent flames. In these approaches, the turbulence affects the flamelet structure through the strain-rate a experienced by the flamelet, or through the scalar dissipation rate χ.

We report results of direct numerical simulations of turbulence in which the properties of material surface elements are studied. In particular, statistics of strain rate and scalar dissipation on the surface elements are extracted.

A close quantitative correspondence between the simulations and turbulent flames cannot be claimed. The flames occur in inhomogeneous flows, and there are large property variations around the flamelets. On the other hand the simulations are of constant-property homogeneous, isotropic turbulence. Further, a material surface provides only a limiting approximation to a propagating surface or to a constant-property surface, corresponding to premixed or diffusion flamelets, respectively. Nevertheless, in spite of these shortcomings, the information presented here provides valuable insights into the turbulent processes affecting surfaces—about which little else is known [2].

For turbulent premixed flames (reviewed by Bray [3] and Pope [4]), flamelet combustion oc-

* Current Address: Department of Mechanical Engineering, The Pennsylvania State University, University Park, PA 16802.

0010-2180/90/$03.50

curs when the laminar flame thickness δ_L is smaller than the Kolmogorov length scale η. There is ample evidence [5] that in spark ignition engines combustion usually takes place in the flamelet regime. To a good approximation, at any instant the flame is a surface, separating reactants from products, that propagates normal to itself at a speed w relative to the reactants ahead. Thus the flame is a *propagating surface*; whereas if w is zero the surface moves with the fluid and is a *material surface* [6]. To a first approximation the propagating speed is the laminar flame speed u_L, but it can vary significantly due to flame stretch (see, e.g., Ref. 7). Sufficiently large stretch can cause extinction.

With regard to turbulent premixed flames, in this article we primarily address two questions:

1. Under what circumstances does a propagating surface remain close (to a specified extent) to an initially coincident material surface?
2. What is the statistical distribution of strain-rate a on a material surface element?

The strain-rate a is defined to be the total strain-rate in the tangent plane of a material surface element: in incompressible flow, a is the negative of the strain-rate normal to the surface, S_N. The strain-rate a is important for three reasons: it causes the surface area to increase, it can affect the propagation speed w, and sufficiently large (or small) values can cause extinction. Several recent models for premixed flamelet combustion make explicit assumptions about the distribution of a [8–10].

For turbulent diffusion flames (reviewed by Bilger [11, 12]) the simplest model [13] is that reaction is confined to a surface: fuel and oxidant diffuse towards the surface from opposite sides, and are instantly consumed when they meet on the surface. The flame sheet is located on the stoichiometric surface—where the mixture fraction $\xi(\mathbf{x}, t)$ adopts its stoichiometric value ξ_{st}. That is, at time t, the flame sheet is the *constant-property surface* composed of all points $\mathbf{x}$ satisfying

$$\xi(\mathbf{x}, t) = \xi_{st}. \tag{1}$$

Flamelet models of turbulent diffusion flames [14–17] attempt to improve upon the Burke–Schumann model [13] by accounting for the structure of the reaction zone, which has a nonzero thickness even in the limit of infinitely fast reactions [18]. In these models, a central role is played by the scalar dissipation $\chi(\mathbf{x}, t)$

$$\chi \equiv 2D\nabla\xi \cdot \nabla\xi, \tag{2}$$

where D is the molecular diffusion coefficient. With several assumptions, it can be shown [17] that the turbulent flamelet properties are uniquely determined by ξ and χ. In particular, they are the same as those of a laminar flame with the same values of ξ and χ. Such laminar flame properties can be obtained either from measurements [19] or from detailed numerical calculations [20].

One of the basic assumptions mentioned above is that the flamelets are sufficiently thin, so that χ varies little within them. Bilger [18] presents strong arguments to suggest that this approximation is questionable in many flames. A second assumption is that the flame is quasi-static, that is, that it responds instantly to changes in χ. The range of validity of this assumption can be tested by performing detailed calculations of laminar flames with a time-dependent strain-rate $a(t)$, leading to time-dependent $\chi(t)$.

These considerations lead to two additional questions that are addressed in this paper:

3. What is the statistical distribution of χ?
4. What is the statistical nature of the time-dependent strain-rate history $a(t)$ on a surface element?

Above a critical value of χ, i.e., say for $\chi \geq \chi_q$, a laminar diffusion flame cannot sustain itself [21]. Most flamelet models [16, 22] incorporate the assumption that the flamelets are extinguished if χ exceeds χ_q. This provides additional motivation for question 3 above.

The subsequent sections are organized as follows. Section 2 describes the use of Lagrangian data from direction numerical simulations (performed by the present authors [23]) to calculate material surface element properties. In Secs. 3 and 4, numerical results are used to study the questions posed above for premixed (1, 2) and diffu-

sion flamelets (3, 4). Section 5 gives further results on the nature of the two-dimensional straining in the tangent plane of a material surface. In Sec. 6 we summarize the conclusions. Numerical details regarding the calculation of surface element properties and their area-averages are given in the Appendices.

2. DETERMINATION OF SURFACE PROPERTIES

2.1 Direct Numerical Simulations

Lagrangian time series of velocity gradients (following fluid particles) provide the basic input for computing the evolution of surface element properties. The time series obtained from the direct numerical simulations of stationary isotropic turbulence performed by Yeung and Pope [23] are used to obtain statistics describing the straining of material surfaces. These data are obtained by tracking up to 4096 fluid particles through turbulent velocity fields made statistically stationary by low-wavenumber forcing [24].

In each simulation, the Navier–Stokes equations with constant density and viscosity are integrated numerically for about six eddy-turnover times. The Eulerian solution algorithm, which uses a pseudo-spectral numerical method, is based on that of Rogallo [25]. The algorithm of Yeung and Pope [26] is used to track the fluid particles accurately. At each time level and for each particle, the velocity gradients are interpolated from the three-dimensional grid of 128^3 nodes. High-wavenumber Eulerian spectra show [26] that the spectral characteristics of the small scales, which provide the dominant contribution to the velocity gradients, agree well with those of grid-generated turbulence in wind-tunnels. The Taylor-scale Reynolds number (R_λ) range is from 38 to 93.

Detailed information on the simulations is available in Ref. 23.

2.2 Material Surface Element Properties

For reference in later sections, we give here definitions of basic material surface element properties. Details of their calculation are given in Appendix A.

Each infinitesimal material surface element is identified with a material point lying on it, with instantaneous position $\mathbf{X}(t)$ and velocity $\mathbf{U}(t)$. The equation of motion is

$$\frac{d\mathbf{X}(t)}{dt} = \mathbf{U}(t). \tag{3}$$

In view of homogeneity, the initial positions $\mathbf{X}(0)$ are prescribed as uniformly distributed in space. The Lagrangian velocity $\mathbf{U}(t)$ is related to the Eulerian velocity field $\mathbf{u}(\mathbf{x}, t)$ by

$$\mathbf{U}(t) = \mathbf{u}(\mathbf{X}(t), t), \tag{4}$$

and is calculated from the grid-node values of $\mathbf{u}$ by cubic spline interpolation (see Ref. 26). All surface properties are evaluated at the location $\mathbf{X}(t)$.

The area amplification factor $A(t)$ is the ratio of the surface element area to its initial value at $t = 0$, (thus $A(0) = 1$). Let $\mathbf{s}^{(1)}(t)$ and $\mathbf{s}^{(2)}(t)$ be infinitesimal material line vectors that span the tangent plane of the surface element, and define

$$\mathbf{A}(t) = \mathbf{s}^{(1)}(t) \times \mathbf{s}^{(2)}(t)/|\mathbf{s}^{(1)}(0) \times \mathbf{s}^{(2)}(0)|. \tag{5}$$

Then the area amplification factor is

$$A(t) = |\mathbf{A}(t)|. \tag{6}$$

The evolution equation for $A(t)$ [2, 6] may be written as

$$\frac{1}{A}\frac{dA}{dt} = a, \tag{7}$$

where a is the total rate of strain in the tangent plane. Since the mean of a is positive (as verified directly by our results), this shows that turbulent stretching produces a continual increase in the mean area of a surface element.

The orientation of the surface is represented by its unit normal, $\mathbf{N}(t)$, given by

$$\mathbf{N} = \mathbf{A}/A. \tag{8}$$

The evolution equation for $\mathbf{N}$ has also been derived by Pope [6]. However, for the present purposes it is simpler instead to determine the evolution of

$\mathbf{s}^{(1)}$ and $\mathbf{s}^{(2)}$ (see Appendix A), and then use Eqs. 5 and 8 directly.

The straining experienced by the surface depends on the local strain-rate tensor $\mathbf{S}$ and the orientation of the surface relative to it. The components of $\mathbf{S}$ are

$$S_{ij} = \frac{1}{2}\left(\frac{\partial u_i}{\partial x_j} + \frac{\partial u_j}{\partial x_i}\right), \tag{9}$$

evaluated at the location $\mathbf{X}(t)$. We are mainly (except in part of Sec. 2) interested in analyzing stationary time series. The velocity gradient time series are stationary, but material surface properties become stationary only after the orientation $\mathbf{N}$ of the surface elements (relative to $\mathbf{S}$) attains a statistically stationary distribution. In analyzing the stationary distribution, the early transients (prior to attainment of stationarity) are disregarded. Therefore, initial values used in the evolution equations (e.g., that of χ) need not be physically significant but are chosen to be close to steady-state mean values in order to hasten the attainment of stationarity.

From plots of the evolution of the means and variances of primary surface properties such as the strain-rate a and scalar dissipation χ, a time level t_0 is selected such that stationarity may be assumed at all later times $t \geq t_0$. The time series beyond t_0 are processed in the same manner as in Yeung and Pope [23]. The length T_0 of the truncated time series (about 2/3 to 3/4 of the total length) varies between $31\tau_\eta$ and $47\tau_\eta$, where τ_η is the Kolmogorov time scale. This is sufficiently long compared to the integral time scales of a and χ (about $1\tau_\eta$ and $4\tau_\eta$ respectively).

The straining of a material surface is most conveniently described in a moving and rotating Cartesian coordinate system, with origin at $\mathbf{X}(t)$, and $\mathbf{N}(t)$ being one of the coordinate directions—the third direction, say. As described in Appendix A, the rate of strain normal to the surface, S_N, is then readily obtained by transforming $\mathbf{S}$ (in fixed axes) to the moving axes, as $\mathbf{S}'$. If the remaining directions (1 and 2) are chosen to be the principal axes of the strain rate in *the tangent plane*, then the rate of strain tensor $\mathbf{S}'$ takes the form

$$\mathbf{S}' = \begin{bmatrix} S_1 & 0 & S'_{13} \\ 0 & S_2 & S'_{23} \\ S'_{31} & S'_{32} & S_N \end{bmatrix}. \tag{10}$$

The axes are chosen so that the principal strain rates in the tangent plane, denoted by S_1 and S_2, are ordered, i.e., $S_1 \geq S_2$. It is important to distinguish between these principal strain rates in the tangent plane from the principal strain rates of the full three-dimensional strain-rate tensor.

For the incompressible flow considered, the continuity equation yields

$$a \equiv S_1 + S_2 = -S_N. \tag{11}$$

2.3 Area-Weighting of One-Time Statistics

If ϕ is a property defined on a surface, then we denote by $\langle \phi(t) \rangle_A$ the area-weighted mean of ϕ on the surface at time t. Area-weighting simply means that equal areas contribute equally to the mean. For an infinite surface, $\langle \phi(t) \rangle_A$ is the area-average of ϕ. In general, area-weighted statistics are the natural and physically-relevant statistics to consider.

In the simulations with M surface elements, the elements are initially (at $t = 0$) ascribed equal infinitesimal areas. At time t, the area of the element has increased by the factor $A(t)$. Hence the area-weighted mean of ϕ is

$$\langle \phi(t) \rangle_A = \frac{\langle A(t)\phi(t) \rangle}{\langle A(t) \rangle}, \tag{12}$$

where $\langle A(t) \rangle$ is the average area at time t, and $\langle\ \rangle$ denotes the expectation of the element property. From the M surface elements, the estimate $\overline{\phi(t)}_A$ for $\langle \phi(t) \rangle_A$ is the area-weighted sample mean

$$\overline{\phi(t)}_A = \frac{1}{M}\sum_{i=1}^{M} w_i(t)\phi_i(t), \tag{13}$$

where the weight assigned to a given element is

$$w_i(t) = A_i(t)/\langle A(t) \rangle. \tag{14}$$

An examination of the statistical nature of the area $A(t)$ indicates that direct application of Eqs. 13 and 14 at large times can result in large statistical errors. We note that the standard error of $\overline{\phi(t)}_A$ depends heavily on the variance var(w) of the weights in Eq. 13. If w_i and ϕ_i are assumed to be uncorrelated (with each other and between different surface elements), then the standard error of $\overline{\phi(t)}_A$ is greater than that of the unweighted value $\overline{\phi(t)}$ (the simple arithmetic mean of $\phi(t)$) by a factor of $\sqrt{\text{var}(w)}$. As shown in Appendix B, for the weights specified by Eq. 14, var(w) increases approximately exponentially with time—and so does the standard error. In Appendix B, we discuss this difficulty further, and present a strategy which largely overcomes it.

Similar considerations of area-weighting also apply to the calculation of other one-time statistics, such as variances and probability densities. In fact, the statistical errors increase with the order of the moments involved, and are greater than that for mean values.

3. PREMIXED FLAMELETS

3.1 Distance Between a Flamelet and a Material Surface

We first address the question raised in the Introduction: under what circumstances does a propagating surface (e.g., a premixed flamelet) remain close to an initially coincident material surface?

Figure 1 is a sketch at time $t > 0$ of a propagating surface and a material surface that were (by construction) coincident at time $t = 0$. The general surface point M on the material surface has position $\mathbf{X}_M(t)$ and normal $\mathbf{N}_M(t)$ (pointing in the direction of propagation of the propagating surface). Let P be the point on the propagating surface intersected by the normal from M. The position and normal at P are $\mathbf{X}_P(t)$ and $\mathbf{N}_P(t)$. The distance between M and P is $z(t)$:

$$z(t) = \mathbf{N}_M(t) \cdot (\mathbf{X}_P(t) - \mathbf{X}_M(t)). \tag{15}$$

For $w = 0$, the two surfaces are identical, and z is zero. There is every reason to suppose, therefore, that if w is sufficiently small, then z is small

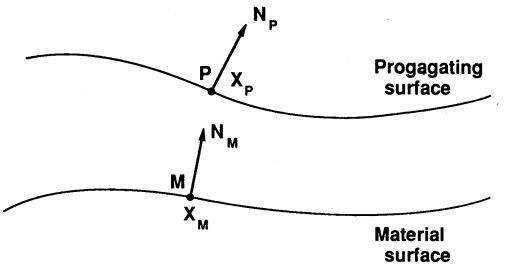

Fig. 1. Sketch of a propagating surface at time $t > 0$ and an initially coincident material surface. The normal $\mathbf{N}_M$ intersects P: the distance between M and P is z.

compared to any relevant length scale. The Kolmogorov length scale η underestimates the smallest turbulence length scale (see, e.g., Ref. 4). Instead, without rigor, we take 5η to characterize the size of the smallest turbulent motions. For sufficiently small w, z is less than 5η, and it can be assumed that

1. the surfaces are approximately parallel (i.e., $\mathbf{N}_P \approx \mathbf{N}_M$); and
2. the velocity field is linear over the distance z.

Making these assumptions we deduce, below, the conditions under which z is indeed small compared to 5η. In view of the assumptions made, these conditions are sufficient, but possibly not necessary.

The point M is a material point and hence we have

$$\frac{d\mathbf{X}_M(t)}{dt} = \mathbf{U}_M(t) \equiv \mathbf{u}(\mathbf{X}_M[t], t). \tag{16}$$

The velocity of the point P has three contributions: the fluid velocity $\mathbf{U}_P(t) \equiv \mathbf{u}(\mathbf{X}_P[t], t)$; the propagation velocity $w\mathbf{N}_P$; and a velocity $\mathbf{V}_T$ in the tangent plane that moves the point P along the surface so that $\mathbf{N}_M$ intersects the surface at P. Thus

$$\frac{d\mathbf{X}_P}{dt} = \mathbf{U}_P + w\mathbf{N}_P + \mathbf{V}_T. \tag{17}$$

(Note that because of $\mathbf{V}_T$, P is not a surface point as defined in Ref 6.)

From the above three equations we obtain

$$\frac{dz}{dt} = \mathbf{N}_M \cdot (\mathbf{U}_P - \mathbf{U}_M) + w\mathbf{N}_M \cdot \mathbf{N}_P + \mathbf{N}_M \cdot \mathbf{V}_T. \tag{18}$$

Invoking assumption (2) above, the first term becomes

$$\mathbf{N}_M \cdot (\mathbf{U}_P - \mathbf{U}_M) = \mathbf{N}_M \cdot (z\mathbf{N}_M \cdot \nabla\mathbf{u}) = S_N z, \tag{19}$$

where

$$S_N \equiv \mathbf{N}_M \cdot (\mathbf{N}_M \cdot \nabla\mathbf{u}) = -a,$$

is the rate of strain normal to the material surface and a is the (total) rate of strain in the tangent plane.

Let θ be the small angle between $\mathbf{N}_M$ and $\mathbf{N}_P$. Then the second term in Eq. 18 is

$$w\mathbf{N}_M \cdot \mathbf{N}_P = w \cos\theta = w(1 + O(\theta^2)). \tag{20}$$

For the final term in eq. 18, since $\mathbf{V}_T$ is normal to $\mathbf{N}_P$, we have

$$\mathbf{N}_M \cdot \mathbf{V}_T = |\mathbf{V}_T| \sin\theta = |\mathbf{V}_T| O(\theta). \tag{21}$$

(A more detailed analysis yields

$$\mathbf{N}_M \cdot \mathbf{V}_T = z\mathbf{N}_M{}^T \cdot \mathbf{S} \cdot (\mathbf{N}_P - \mathbf{N}_M) + O(\theta^2),$$

where $\mathbf{N}_M{}^T$ is the transpose of $\mathbf{N}_M$, and $\mathbf{S}$ is the strain-rate tensor.)

Combining the above results, and neglecting terms of order θ or higher, we obtain the simple expression

$$\frac{dz}{dt} = -az + w. \tag{22}$$

The first term represents the action of straining to draw the point P close to M (for $a > 0$); the second term represents the propagation of P away from M.

We would be satisfied to take w as a constant. But the analysis becomes no more difficult if we let w depend linearly on the strain-rate a. According to both theory [27] and experiment [7], this is a realistic assumption for plane flames. Hence we take

$$w = w_0 + a\mathfrak{L}, \tag{23}$$

where w_0 is the (unstrained) laminar flame speed and $\mathfrak{L}$ is the Markstein length [21, 28].

Substituting Eq 23 into Eq. 22 we obtain

$$\frac{dz^*}{dt^*} = -a^*(z^* - \mathfrak{L}^*) + w_0^*, \tag{24}$$

where asterisks denote normalization by the Kolmogorov length (η), velocity (v_η), or time (τ_η) scales. Finally, defining

$$Z \equiv (z^* - \mathfrak{L}^*)/w_0^*, \tag{25}$$

we obtain

$$\frac{dZ}{dt^*} = 1 - a^*Z. \tag{26}$$

Time series of the strain rate $a^*(t^*)$ are obtained from direct numerical simulations, and then Eq. 26 is integrated to yield the time series of $Z(t^*)$. The initial condition used is $Z(0) = 0$, which, it should be noted, is equivalent to $z = \mathfrak{L}$. Two observations from the numerical results are (1) that Z becomes stationary (as expected since a^* is predominantly positive), and (2) that $Z(t^*)$ varies little with R_λ, since $a^*(t^*)$ varies little. Consequently, $Z(t^*)$ is essentially universal since it is independent of w_0, $\mathfrak{L}$, and the Kolmogorov scales. Note also (from Eq. 26) that Z cannot become negative.

Before presenting the numerical results we make several deductions from the universality of $Z(t^*)$ and from the relation

$$z/\eta = \mathfrak{L}/\eta + Zw_0/v_\eta, \tag{27}$$

which is readily obtained from Eq. 25:

a. The Kolmogorov velocity scale v_η, rather than the turbulence intensity u', provides the appropriate scaling for w_0 (in this context). [We note that from the isotropic turbulence relation

(e.g., Ref. 30)

$$\langle \epsilon \rangle = 15\nu \langle (\partial u_1/\partial x_1)^2 \rangle = 15\nu u'^2/\lambda^2, \qquad (28)$$

where $\langle \epsilon \rangle$, ν, and λ are the mean dissipation rate, kinematic viscosity, and Taylor microscale, respectively, it may be readily shown that

$$v_\eta/u' = 15^{1/4} R_\lambda^{-1/2}.$$

This ratio is 0.32 at R_λ 38 and 0.20 at R_λ 93.]

b. The separation distance z varies linearly with w_0.
c. The dependence of w on a increases z by precisely the Markstein length.
d. For the (impractical) case $w_0 = 0$ (but $\mathcal{L} \neq 0$), the flame becomes separated from the material surface by a *fixed* distance equal to $\mathcal{L}$. (This last fascinating deduction cannot legitimately be made from Eq. 27, but rather comes from the solution to Eq. 24:

$$z(t) = \mathcal{L} + (z(0) - \mathcal{L}) \exp\left\{ \int_0^t -a(s)\, ds \right\}. \qquad (29)$$

Since a is predominantly positive, the exponential term tends rapidly to zero.)

Figure 2 shows the pdf of Z when it has achieved a statistically stationary state. The pdf is shown for two Reynolds numbers ($R_\lambda = 38$ and $R_\lambda = 93$), and is area-weighted. Moments of Z and ln Z are given in Table 1 for all four Reynolds numbers. The significance of the distribution can be interpreted through Eq. 27. For example, for $\mathcal{L} = 0$ and $w_0 = v_\eta$, the distance is $z = Z\eta$. Thus, it may be seen from Fig. 2 that (for this case) the most probable value of z is about 2η.

The shape of the pdf appears approximately log-normal. Figure 3 shows, for four Reynolds numbers, the standardized pdfs of ln Z. It may be seen that small values of Z are less probable than for a log-normal distribution (the dashed line); the converse is true for large values. Equivalently, the skewness coefficient of ln Z is positive (Table 1). The considerable statistical errors evident in Fig. 3 do not allow a firm statement on the Reynolds-number dependence (if any).

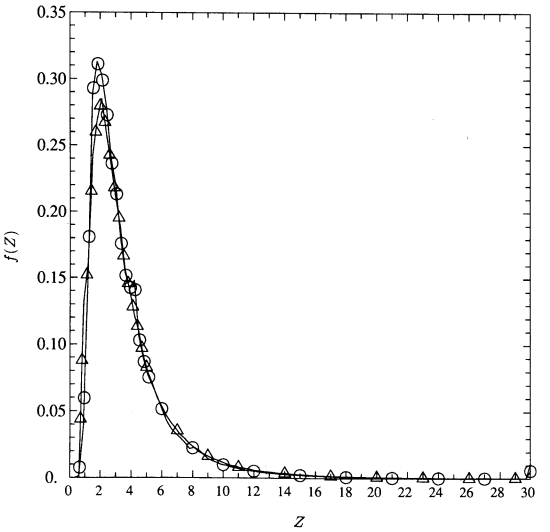

Fig. 2. Stationary-case pdf (area-weighted) of normalized distance Z between material and propagating surfaces, at R_λ 38 (Δ) and R_λ 93 (○). (Note that values at the end-points include contributions from samples lying beyond the range shown.)

The next two figures examine the evolution of $Z(t)$ from the initial condition $Z(0) = 0$. Figure 4 shows the evolution of the area-weighted ($\langle Z(t) \rangle_A$) and unweighted ($\langle Z(t) \rangle$) means of $Z(t)$, for the same two Reynolds numbers considered in Fig. 2. It may be seen that $\langle Z(t) \rangle_A$ approaches an asymptotic value of about 3.5, whereas $\langle Z(t) \rangle$ increases beyond 9. This large difference clearly

TABLE 1

Moments of Z and ln Z (Sec. 3.1: Stationary Case)[a]

R_λ	38	63	90	93
$\langle Z \rangle_A$	3.84	4.24	3.76	3.78
$\mathrm{var}_A(Z)$	12.4	12.0	10.5	9.6
$P^A(Z<5)$	0.787	0.744	0.797	0.791
$\mathrm{var}_A(\ln Z)$	0.384	0.378	0.374	0.346
$\mu_3{}^A(\ln Z)$	0.372	0.429	0.602	0.534
$\mu_4{}^A(\ln Z)$	3.20	3.10	3.42	3.27

[a] All quantities are area-weighted. Skewness coefficients and flatness factors are denoted by μ_3 and μ_4, respectively.

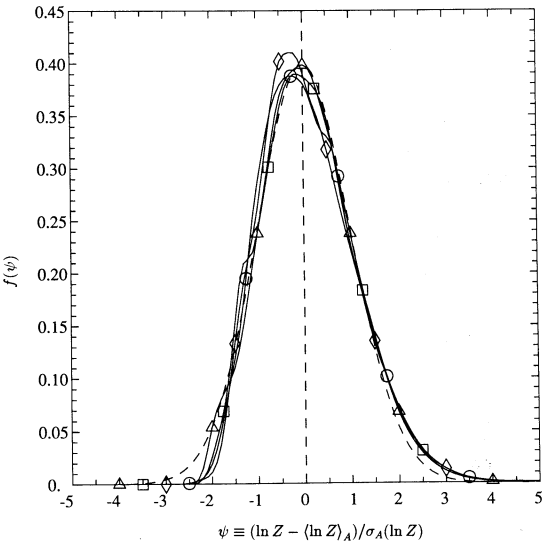

Fig. 3. Stationary-case standardized pdf (area-weighted) of the logarithm of the normalized distance Z between material and propagating surfaces, at four Reynolds numbers. ΔR_λ 38; $\square$ R_λ 63; $\diamondsuit R_\lambda$ 90; $\bigcirc R_\lambda$ 93. Dashed curve (partly hidden) represents standard Gaussian density. [Note that in this and other similar plots, σ is the standard deviation and ψ denotes a standardized random variable, with pdf $f(\psi)$.]

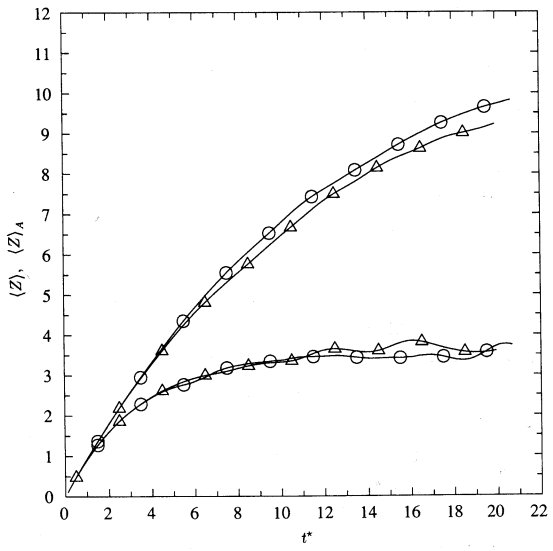

Fig. 4. Growth of mean normalized distance Z between initially coincident material and propagating surfaces, in Kolmogorov-scaled time ($t^* \equiv t/\tau_\eta$) at R_λ 38 (Δ) and R_λ 93 ($\bigcirc$). Lower curves—area-weighted; upper curves—unweighted.

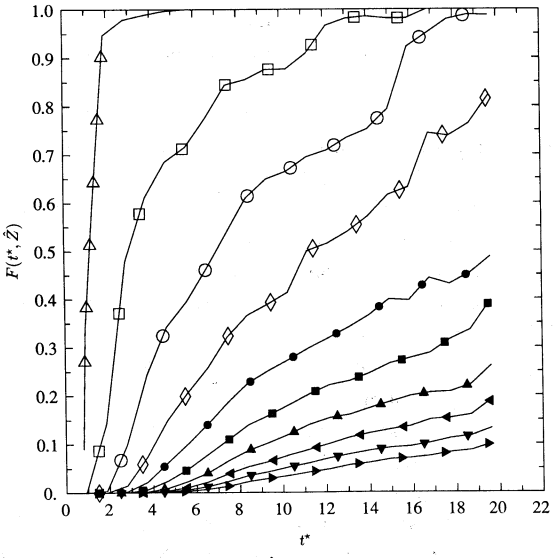

Fig. 5. The function $F(t^*, \hat{Z})$ (Sec. 3.1) from R_λ 93 data. Range of $\hat{Z}$ shown is from 1 (Δ), 2... to 10 ($\blacktriangle$).

emphasizes the need to distinguish between the two means. Because large strains a tend to decrease Z (Eq. 26) and to increase A (Eq. 7), it is expected—and is observed—that $\langle Z \rangle_A$ is less than $\langle Z \rangle$.

The linear analysis embodied in Eq. 22 is valid at sufficiently small time for any w and $\mathcal{L}$, but breaks down once z/η becomes too large. To quantify the time to this breakdown, Fig. 5 shows the function $F(T^*, \hat{Z})$, which is the (area-weighted) fraction of flame elements for which Z exceeded $\hat{Z}$ at any time before t^*. This statistic is subject to considerable statistical variability, especially at large t^*, because the number of available realizations is limited. Nevertheless, it may be seen, for example, that it takes at least about 16 Kolmogorov time scales for half of the flamelets to exceed $\hat{Z} = 5$ ($F(16, 5) \approx 1/2$ and $F(20, 5) \approx 1/2$ for the R_λ 38 and R_λ 93 simulations respectively).

The above analysis and results have been presented to determine when a propagating surface remains close to an initially-coincident material surface. The two surfaces are deemed to be close if the distance $z(t)$ between them is less than 5η. The following conclusions can be drawn:

i. z/η is given by Eq. 27 in which $Z(t^*)$ is a uni-

versal stochastic function, being independent of w_0, $\mathcal{L}$, and (to an excellent approximation) R_λ.

ii. The Kolmogorov velocity scale provides the appropriate normalization for the laminar flame speed. The condition $w_0/v_\eta \ll 1$ is certainly sufficient to satisfy $z < 5\eta$ (whereas $w_0/u' \ll 1$ may not be).

iii. In the steady state, for $\mathcal{L} = 0$ and $w_0 = v_\eta$, z is less than 5η with probability approximately 0.8 (Table 1).

iv. For the same conditions as iii, it takes slightly longer than 16 Kolmogorov time scales for half of the flamelets (area-weighted), evolving from the initial condition $z = 0$, to exceed $z = 5\eta$.

v. In the steady state, the dependence of flame speed on stretch increases z by precisely the Markstein length $\mathcal{L}$.

3.2 Statistical Distribution of Strain Rate in the Tangent Plane

The strain rate in the tangent plane, a, is important because it causes area changes (Eq. 7), because the laminar flame speed can depend on it, and because sufficiently large values of $|a|$ can cause extinction. In each case, the relevant statistics are the area-weighted statistics of a. For comparison we also present unweighted statistics of a, and unweighted statistics of α—defined to be the strain rate on a randomly oriented[1] area element.

For any surface element—material, propagating, or fixed—the one-time statistics of the strain rate in the tangent plane (a_T) depends on the orientation of the element (characterized by its normal **N**) relative to the strain-rate tensor. (The symbol a_T pertains to any surface element, whereas a pertains to a material surface element.) For example, a_T can be determined from the principal strain rates and the orientation between **N** and the principal axes of the strain-rate tensor.

In isotropic turbulence, the strain-rate for a randomly oriented surface element ($\alpha \equiv a_T$) is statistically identical to that on a fixed element, since the strain-rate tensor is randomly oriented. Thus (in view of the continuity equation) α is statistically identical to $-\partial u_1/\partial x_1$ (for any choice of fixed coordinate system). Note that α has zero mean, but its distribution is not symmetrical: its skewness coefficient μ_3 is found to be 0.5, in agreement with Kerr [30]. In analogy to Eq. 7, the area A_f of a fixed surface element evolves by

$$\frac{1}{A_f}\frac{dA_f}{dt} = \alpha. \tag{30}$$

It thus follows that $\langle \ln A_f \rangle$ is constant while $\langle A_f \rangle$ increases monotonically with time (since $\langle \exp(\alpha) \rangle$ is greater than $\exp\langle \alpha \rangle$ for any random variable α with nonzero variance).

A material surface element is not randomly oriented relative to the strain-rate tensor, and hence the strain rate in the tangent plane ($a \equiv a_T$) differs from α.

A propagating surface element is also reoriented by the velocity gradients, which are of order τ_η^{-1}. This results in a preferential orientation with the strain-rate tensor only if the strain rate is persistent—that is, only if it changes on a time scale that is not small compared to τ_η. For a material surface ($w = 0$) the time scale of change is of order τ_η (see Sec. 4). And a slowly propagating surface ($w \leq v_\eta$) is well approximated by a material surface element, and consequently the straining it experiences is well approximated by a. But the strain rate following a rapidly propagating surface changes on a time scale η/w (i.e., the time it takes the surface to propagate a distance η, which is the order of the correlation length of the strain-rate field). Thus for $\eta/w \ll \tau_\eta$, which is equivalent to $w \gg v_\eta$, the straining is too fleeting for preferential orientation to occur, and the strain rate in the tangent plane a_T is statistically the same as that on a randomly oriented surface, i.e., α. For the same reason, the area of a rapidly propagating surface is statistically independent of its current strain rate, and thus its area weighted and unweighted statistics are equal.

In summary, the straining on a slowly propagating surface ($w \leq v_\eta$) is well represented by that on a material surface, a. The distribution

[1] For a surface element with normal N, the term "randomly-oriented" is used to indicate that N is uniformly distributed on the unit sphere.

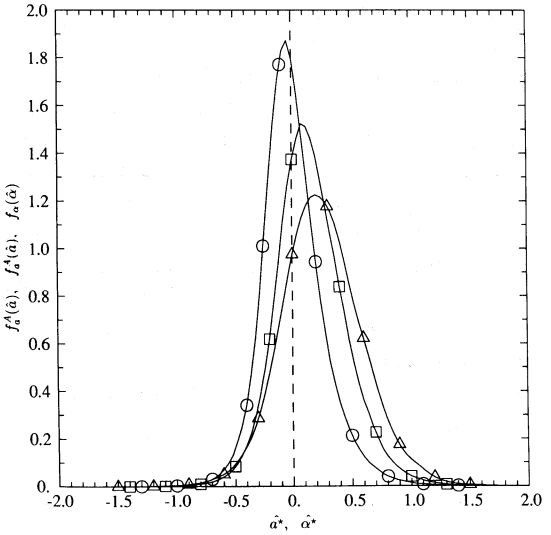

Fig. 6. Probability densities of Kolmogorov-scaled strains acting on material and fixed surfaces, for the R_λ 93 case. Δ a^* (area-weighted, slightly smoothed); $\square$ a^* (unweighted); $\circ$ α^* (for fixed surfaces).

TABLE 2

Moments of the Strains a and α (Sec. 3.2)[a]

R_λ	38	63	90	93
$\langle a^* \rangle_A$	0.287	0.275	0.273	0.283
$\langle a^* \rangle$	0.162	0.152	0.146	0.153
$P^A(a<0)$	0.195	0.202	0.195	0.191
$P(a<0)$	0.297	0.305	0.299	0.298
$P(\alpha<0)$	0.535	0.533	0.533	0.535
$\mathrm{var}_A(a^*)$	0.118	0.119	0.115	0.116
$\mathrm{var}(a^*)$	0.091	0.087	0.080	0.086
$\mathrm{var}(\alpha^*)$	0.066	0.065	0.066	0.066
$\mu_4{}^A(a)$	3.30	3.34	3.25	3.37
$\mu_4(a)$	3.15	3.21	3.15	3.17
$\mu_4(\alpha)$	4.23	4.65	5.23	4.75
$\mu_3(\alpha)$	0.50	0.48	0.49	0.50

[a] Subscript or superscript A denotes area-weighted quantities.

of strain rate on such a surface is denoted by $f_a{}^A(\hat{a})$—the area-weighted pdf of a. For a rapidly propagating surface ($w \gg v_\eta$), the straining is given by α—the strain rate on a randomly oriented (or fixed) area element. The pdf of α is given by $f_\alpha{}^A(\hat{\alpha}) \approx f_\alpha(\hat{\alpha})$—the area-weighted or the unweighted pdf of α. Thus $f_a{}^A(\hat{a})$ and $f_\alpha(\hat{\alpha})$ can be regarded as the limiting distributions of strain-rate for slowly and rapidly propagating surfaces respectively. For comparison, the unweighted pdf of a—$f_a(\hat{a})$—is also presented.

The three pdfs, $f_a{}^A(\hat{a}), f_a(\hat{a})$ and $f_\alpha(\hat{\alpha})$ are shown in Fig. 6 for $R_\lambda = 93$, with a and α normalized by τ_η. Some of the important characteristics of these pdfs are given in Table 2, from which it may be seen there is virtually no Reynolds-number dependence. We note that relative to $f_a(\hat{a}), f_a{}^A(\hat{a})$ is displaced to the right, since large areas are associated with strong stretching (positive a).

The mean $\langle \alpha \rangle$ is identically zero, whereas $\langle a^* \rangle_A$ is approximately 0.28, nearly twice the unweighted mean $\langle a^* \rangle$ (approximately 0.15). We also note that the observed variance of $\alpha^*(\equiv \alpha\tau_\eta)$ is close to its theoretical value of 1/15, which results from the isotropic turbulence relation given by Eq. 28. Although in the mean a material surface is stretched (i.e., $\langle a \rangle_A > 0$), nevertheless, there is 20% probability that a is negative. This indicates the possibility, for some fuel–air mixtures, of extinction by negative straining—as occurs in open-tipped Bunsen flames (see, e.g., Ref. 31).

Again in view of the possibility of extinction, it is useful to examine the probabilities of large and small strain rates—i.e., the tails of the pdfs. The tails are emphasized by showing, in Fig. 7, the logarithms of the pdf's given in Fig. 6. Far from the origin, the logarithms decrease linearly (most markedly so for $f_\alpha(\hat{\alpha})$), rather than parabolically (as in the case of a Gaussian pdf). Velocity gradients are intermittent and non-Gaussian. Figure 7 shows that $f_\alpha(\hat{\alpha})$ deviates further from a Gaussian density than do $f_a{}^A(\hat{a})$ and $f_a{}^A(\hat{a})$. The flatness factor of α is also much higher (Table 2).

It may also be seen that at large a^*, say for $a^* > 1, f_a{}^A(\hat{a})$ is about 3 times the value of $f_a(\hat{a})$. Thus, using the unweighted pdf to estimate the probability of extinction due to high flame stretch can yield a value that is too low by as much as a factor of 3. The effect of area-weighting is particularly pronounced for large a^*, since high stretch is associated with large sureface areas. For

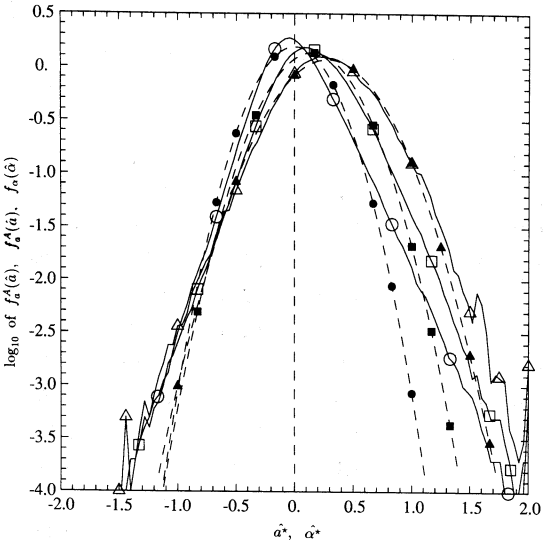

Fig. 7. Based-10 logarithms of the pdfs shown in Fig. 6 (but without smoothing for the area-weighted pdf of a^*). Dashed parabolic curves with the corresponding (see Fig. 6) solid symbols represent Gaussian densities with the observed means and variances.

negative straining the difference between $f_a{}^A(\hat{a})$ and $f_a(\hat{a})$ is much less; both pdfs indicate negligible probability for $a^* < -1.5$.

The nature of the principal components of a, i.e., S_1 and S_2, is examined in Sec. 5.

4. DIFFUSION FLAMELETS

4.1 The Diffusive Layer: Model and Results

We consider a conserved passive scalar $\xi(\mathbf{x}, t)$—analogous to the mixture fraction—governed by the equation

$$\frac{\partial \xi}{\partial t} + \mathbf{u} \cdot \nabla \xi = D \nabla^2 \xi, \tag{31}$$

in homogeneous isotropic turbulence. The initial condition is that there are blobs of fluid with $\xi = 1$, surrounded by fluid with $\xi = 0$. Material surfaces are defined (initially) by interfaces between blobs and the surrounding fluid; and the initial blob geometry is such that all length scales (e.g., size, separation distance, surface radii of curvature) are large compared to the Kolmogorov scale, η.

Because of the initial differences in ξ, diffusive layers of thickness $\delta(t)$ (defined below) develop around the material surfaces. Provided that $\delta(t)$ is small (compared to other length scales), the mixing near each point on the material surfaces can be well approximated as a transient one-dimensional diffusion process (normal to the surface) in a uniform straining field. To show this, we rewrite Eq. 31 in a coordinate system attached to the material surface. Let the (moving) origin M be a material point, and let the (rotating) axes be chosen such that $y = x_3'$ is the coordinate in the direction of the normal to the surface (pointing into the blobs); see Fig. 8. In this coordinate system Eq. 31 becomes

$$\frac{\partial \xi}{\partial t} + (\mathbf{u}(\mathbf{x}) - \mathbf{u}(0)) \cdot \nabla \xi = D \nabla^2 \xi, \tag{32}$$

Now gradients in the x_1' and x_2' directions are negligibly small compared to those in the $y = x_3'$ direction. And since, by assumption, δ is much smaller than η, the velocity field can be taken to be linear. Hence Eq. 32 becomes, to a good approximation,

$$\frac{\partial \xi}{\partial t} - ay \frac{\partial \xi}{\partial y} = D \frac{\partial^2 \xi}{\partial y^2}, \tag{33}$$

where, as before, $a(t)$ is the rate of strain in the tangent plane at the material point $y = 0$; and use has been made of the incompressibility condition $S_N = -a$.

Let L be the distance in the direction of $\pm y$ to the nearest neighboring material surface (Fig. 8). Now provided $\frac{1}{2} L$ is much larger than δ, boundary conditions appropriate to Eq. 33 are

$$\xi\left(\frac{1}{2} L, t\right) = 1, \qquad \xi\left(-\frac{1}{2} L, t\right) = 0. \tag{34}$$

In this case ($L \gg \delta$), the solution to Eqs. 33–34 in the region $-\frac{1}{2} L < y < \frac{1}{2} L$ is little affected if the boundary conditions are, instead, taken as

$$\xi(\infty, t) = 1, \qquad \xi(-\infty, t) = 0. \tag{35}$$

In summary, to a good approximation, the mixing field close to the material surface is described by Eq. 33 with the boundary conditions (Eq. 35)

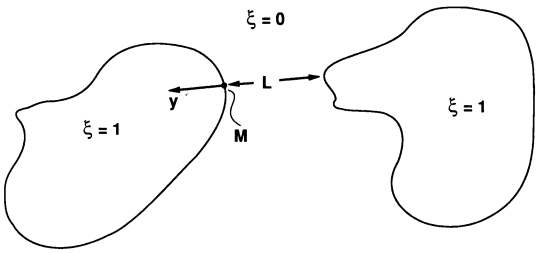

Fig. 8. Sketch of diffusive layers (lines) between blobs of concentration $\xi = 1$ and $\xi = 0$.

provided that

i. δ/η is sufficiently small for the velocity field to be linear over distances of order δ,
ii. δ is small compared to the radii of curvature of the surface, so that derivatives in the tangent plane are negligible, and,
iii. the distance L between neighboring diffusive layers is large compared to δ, so that there are regions of uniformity ($\xi = 0$ or 1) in between.

All three assumptions are satisfied for sufficiently small times; i is always satisfied if the Schmidt number $\mathrm{Sc} \equiv \nu/D$ is sufficiently large; but after some time iii is no longer satisfied, since the action of turbulence is to continually strain and fold the surfaces, thus reducing L, eventually exponentially on the Kolmogorov time scale.

The initial profile of ξ is a Heaviside unit step function at $y = 0$. With boundary conditions given by Eq. 35, the exact solution to Eq. 33 has a self-similar form

$$\xi(y, t) = \frac{1}{\delta\sqrt{2\pi}} \int_{-\infty}^{y} \exp(-z^2/2\delta^2)\, dz, \tag{36}$$

which is an error function profile:

$$\xi(y, t) = \frac{1}{2}\,[1 + \mathrm{erf}(y/\sqrt{2}\delta(t))], \tag{37}$$

with the thickness $\delta(t)$ evolving according to the ordinary differential equation

$$\frac{d\delta^2}{dt} = -2a(t)\delta^2 + 2D. \tag{38}$$

This equation may be rewritten in normalized form as

$$\frac{d\delta^{*2}}{dt^*} = -2a^*\delta^{*2} + 2,$$

where $a^* \equiv a\tau_\eta$ and $t^* \equiv t/\tau_\eta$ and δ is normalized by the Batchelor length scale l:

$$\delta^* = \delta/l,$$

where

$$l \equiv \eta/\mathrm{Sc}^{1/2} \equiv \eta(D/\nu)^{1/2}. \tag{39}$$

(Note that the quantity $D\tau_\eta/l^2$ is unity.)

The scalar dissipation (Eq. 2), is readily evaluated from Eq. 36:

$$\chi(y, t) \equiv 2D\left(\frac{d\xi}{dy}\right)^2 = \frac{D}{\pi\delta^2}\exp(-y^2/\delta^2). \tag{40}$$

Its maximum value over the diffusive layer occurs at the origin (on the material surface), and is denoted by χ_0:

$$\chi_0 = D/\pi\delta^2. \tag{41}$$

Substituting Eq. 41 into Eq. 38 and scaling by τ_η yields the evolution equation for $\chi_0^* \equiv \chi_0\tau_\eta$ as

$$\frac{d\,\ln\chi_0^*}{dt^*} = 2a^* - 2\pi\chi_0^*. \tag{42}$$

This equation is integrated numerically to obtain $\chi_0^*(t^*)$ and then $\delta^*(t^*)$ is calculated from Eq. 41. It may be noted that the steady-state solution

$$\chi_0^* = a^*/\pi. \tag{43}$$

exists only if a^* is a positive constant.

We now address questions 3 and 4 posed in the Introduction, by examining the statistics of δ^* and χ_0^* is relation to the strain-rate history $a(t)$, which governs their evolution.

Figure 9 shows the (area-weighted) pdf of the normalized diffusive layer thickness δ^* for two Reynold numbers, R_λ 38 and 93. There is apparently little Reynolds-number dependence. T

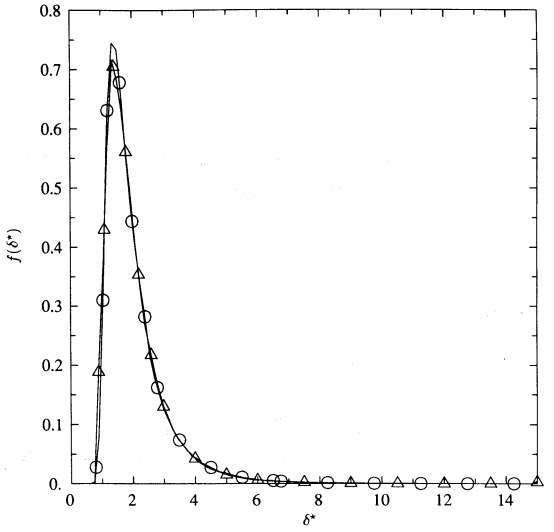

Fig. 9. Probability density of normalized diffusive layer thickness δ^* for R_λ 38 (Δ) and R_λ 93 ($\bigcirc$) cases.

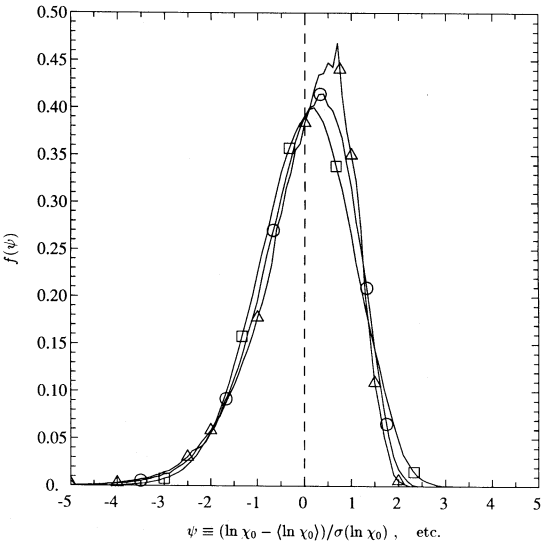

Fig. 10. Standardized pdf of the logarithms of ln χ_0 (Δ, area-weighted; $\square$, unweighted) and ln ϵ_ϕ ($\circ$) at R_λ 93.

pdf is seen to be concentrated in the range 1.0 to 3.0. The mean and standard deviation of δ^* are found to be close to 2.0 and 1.05, respectively, for all Reynolds numbers studied. A sharp drop is observed for small values of δ^*, and there is negligible probability for δ^* less than about 0.75. In such thin layers ($\delta^* \ll 1$) the scalar gradients (and dissipation) are extremely large. Their occurrence is thus inhibited by the smearing effect of molecular diffusion acting at the smallest length scales.

The pdf shown has a high positive skewness, with a long tail indicating small yet measurable probability up to high values. Surface elements satisfying $\delta^* < 5$ and $\delta^* < 10$ account for 97.7% and 99.7% of the total surface area, respectively. These estimates can be seen to provide justification for assumption i of this section for high Schmidt numbers. Under usual laboratory experimental conditions (say 25°C), the Schmidt number for diffusion in liquids is typically of order 1000. Taking Sc to be 1000 in Eq. 39, we find $\delta^* = 5$ and $\delta^* = 10$ correspond to $\delta = 0.16\eta$ and $\delta = 0.32\eta$, respectively. The condition $\delta \ll \eta$ is clearly well satisfied for this case. Even for gases (Sc ≈ 1, $\delta \approx \delta^*\eta$), assumption i appears reasonable: there is only about 2% probability of δ exceeding 5η, which is taken in the previous section to be the length scale of the smallest turbulent motions.

We now examine the statistics of the scalar dissipation χ. It is of interest to determine whether χ is log-normally distributed, as hypothesized for nonnegative small-scale quantities [2] and as observed in direct numerical simulations [32]. Although χ depends on the spatial location within the diffusive layer, i.e., from Eqs. 40–41,

$$\ln \chi = \ln \chi_0 - y^2/\delta^2, \tag{44}$$

it may be seen that, for fixed y/δ, the variance and standardized pdf of ln χ are independent of y/δ.

Figure 10 shows, at R_λ 93, the standardized pdfs of ln χ_0 (area-weighted and unweighted). The logarithms of the same pdfs are given in Fig. 11 compared to the standard Gaussian pdf (dashed line). Table 3 gives the variances, skewness coefficients, and flatness factors (which are the same for ln χ_0 and ln χ_0^*).

It may be seen that the pdf of ln χ_0 is significantly non-Gaussian and negatively skewed. The lack of large values (say 2.5 standard deviations or more above the mean) reflects the sharp drop for $\delta^* < 1$ in the pdf of δ^* (Fig. 9). Area-weighting

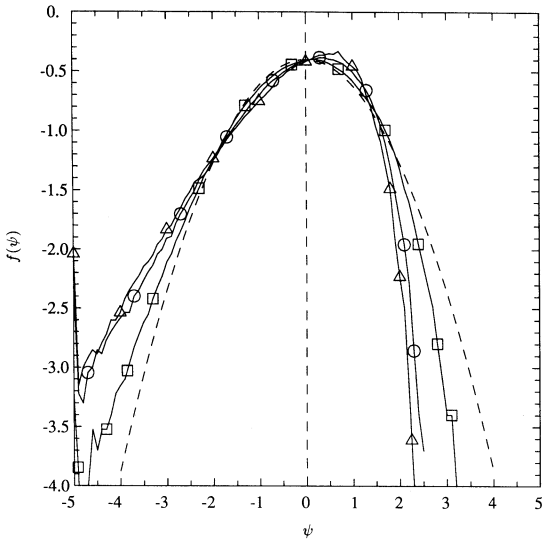

Fig. 11. Base-10 logarithms of the pdfs shown in Fig. 10, compared with the standard Gaussian density.

has only a moderate effect on the shape of this pdf, resulting in increased contributions from the range 0–1.5 standard deviations above the mean. But the area-weighted variance of ln χ_0 is significantly reduced to little more than half of the unweighted value. There is no statistically significant dependence on Reynolds number.

The pdf of ln χ_0 obtained here using the one-dimensional diffusive layer model can be compared with that obtained from direct simulations of the mixing of a conserved passive scalar [32]. In these simulations Eq. 31 was solved for a scalar field $\phi(\mathbf{x}, t)$ with Schmidt number 0.7, and the statistics of the scalar dissipation ϵ_ϕ were extracted. (We use ϕ and ϵ_ϕ to denote scalar properties obtained directly from Eq. 31, whereas ξ and χ denote those obtained from the diffusive-layer model.) The initial scalar fields $\phi(\mathbf{x}, 0)$—the same as used in Ref. 32—consist of equal amounts of blobs of $\phi \approx 1$ and $\phi \approx -1$. No mean scalar gradients are present, and the scalar decays isotropically. A self-similar state is reached, in which (1) the variance and mean dissipation of the scalar decay exponentially with time, and (2) ln ϵ_ϕ maintains an approximately log-normal distribution with a constant variance.

TABLE 3

Moments of Scalar Dissipations: ln χ_0 and ln ϵ_ϕ[a]

R_λ	38	63	90	93
$\text{var}_A(\ln \chi_0)$	0.66	0.69	0.71	0.66
$\text{var}(\ln \chi_0)$	1.19	1.31	1.29	1.31
$\mu_3(\ln \chi_0)$	−0.67	−0.70	−0.69	−0.70
$\mu_4(\ln \chi_0)$	3.68	3.77	3.75	3.79
$\text{var}(\ln \epsilon_\phi)$	2.22	2.42	2.66	2.63
$\mu_3(\ln \epsilon_\phi)$	−0.34	−0.35	−0.29	−0.28
$\mu_4(\ln \epsilon_\phi)$	3.15	3.14	3.04	3.04

[a] For μ_3 and μ_4 of ln χ_0, we give unweighted rather than area-weighted values since the latter (as higher-order moments) are substantially affected by statistical error (but are probably more non-Gaussian).

The pdf of ln ϵ_ϕ in the self-similar state is also shown in Figs. 10 and 11, and its moments are given in Table 3. It may be seen that ϵ_ϕ is closer to log-normal than is χ_0. As the Reynolds number increases, the flatness factor of ϵ_ϕ approaches the Gaussian value, but a negative skewness remains—i.e., very small values resulting from near-zero scalar gradients are more probable than very high values. The variance of ln ϵ_ϕ increase slightly with Reynolds number, and is strikingly larger than that of ln χ_0.

The correspondence is not close between the scalar field $\phi(\mathbf{x}, t)$ from the direct numerical simulations and that ($\xi(\mathbf{x}, t)$) from the diffusive-layer model. For example, the pdf of ϕ is Gaussian, while the assumptions made imply that ξ has close to a double-delta-function distribution (with significant probability close to $\xi = 0$ and $\xi = 1$ only). Nevertheless, the large difference between the variances of ln χ_0 and ln ϵ_ϕ warrants further investigation.

A better—but still rather loose—correspondence between ϵ_ϕ and χ is obtained from the following model: suppose that the $\phi(\mathbf{x}, t)$ field consists of diffusive layers across which ϕ changes by a random amount Δ, and that the distance L between adjacent layers is $\gamma\eta$, where γ is a fixed parameter. Then the scalar dissipation according to this model (denoted by ϵ_m) is readily deduced from Eq. 40:

$$\epsilon_m = \Delta^2 \chi_0 \exp(-z^2/\delta^2), \tag{45}$$

where z is a random variable[2] uniformly distributed in $[-\gamma\eta, \gamma\eta]$. Hence

$$\ln \epsilon_m = \ln \Delta^2 + \ln \chi_0 - C\chi_0^* \gamma^2 \vartheta^2, \quad (46)$$

where $C = \pi \mathrm{Sc}$, and ϑ is uniformly distributed in $[0, 1]$. Approximating $\ln \chi_0^*$ as a normal random variable with mean μ and variance σ^2, and stipulating χ_0, Δ, and ϑ all to be independent, we obtain[3]

$$\begin{aligned}\mathrm{var}(\ln \epsilon_m) &= \mathrm{var}(\ln \Delta^2) + \mathrm{var}(\ln \chi_0^*) \\ &\quad + C\gamma^2 \langle \chi_0^* \rangle_M [C\gamma^2 \langle \chi_0^* \rangle_M \\ &\quad \times \left(\frac{1}{5} e^{\sigma^2} - \frac{1}{9} \right) - \frac{2\sigma^2}{3} \Big], \quad (47)\end{aligned}$$

where $\langle \chi_0^* \rangle_M = \exp(\mu + \sigma^2/2)$ is the mean of χ_0^* in this model.

It may be seen from Eq. 47 that both ingredients in the model—the random difference Δ, and the consideration of the entire interval $[-L, L]$—increase the variance of $\ln \epsilon_m$ above that of $\ln \chi_0$. The first term, $\mathrm{var}(\ln \Delta^2)$, is difficult to estimate: we note only that it is likely to increase with R_λ, as the scalar field becomes more intermittent. This could explain the observed dependence of $\mathrm{var}(\ln \epsilon_\phi)$, but independence of $\mathrm{var}(\ln \chi_0)$, on R_λ. The final term in Eq. 47 shows that the predicted value of $\mathrm{var}(\ln \epsilon_m)$ is extremely sensitive to the value of γ. The plausible choice $\gamma = 3.57$, using $\mathrm{Sc} = 0.7$ and the area-weighted values of μ and σ^2, yields values of $\mathrm{var}(\ln \epsilon_m)$ near 2.45—close to those of $\mathrm{var}(\ln \epsilon_\phi)$ given in Table 3 (with the neglect of $\mathrm{var}(\ln \Delta^2)$). This choice of γ corresponds to $\gamma\eta$ being 3.0 Batchelor scales. Referring to Fig. 9, we note that this covers the thickness of nearly 90% (e.g. 88% in the R_λ 38 case) of the surface areas.

4.2 Relation to Surface-Strain Statistics

We now examine the joint distribution of surface strain a and scalar dissipation χ, and the two-time statistics of a.

[2] Unrelated to the distance between material and propagating surfaces considered in Sec. 3.

[3] Note that the variances of $\ln \chi_0$ and $\ln \chi_0^*$ are identical.

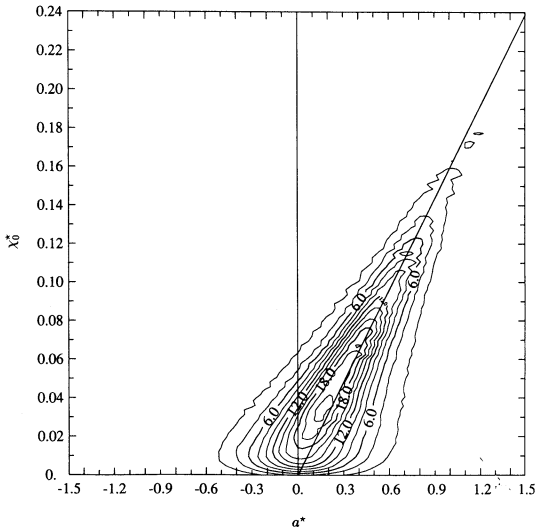

Fig. 12. Contour plot of (area-weighted) joint pdf of Kolmogorov-scaled surface strain a^* and scalar dissipation on surface χ_0^*, from R_λ 93 data. Contour levels are shown multiplied by 100. Contour interval is 0.02. Sloping vertical line represents Eq. 43.

Figure 12 is a contour plot of the joint probability density of a^* and χ_0^*, at R_λ 93. The steady-state solution (Eq. 43) corresponds to the sloping straight line. The quasi-static condition it implies is only of limited applicability, since a fluctuates rapidly (on the Kolmogorov scale) and is not always positive. However, if $a^* > 0$ and the time scale of change of χ_0^* is long (compared to $1/a^*$), then it would be reasonable to assume quasi-static conditions. It may be noted that the most probable value of the ratio between a^* and χ_0^*, as inferred from the line of highest probability, is close to that given by Eq. 43.

The properties of the time series of the surface strain $a(t)$ are important because $a(t)$ determines the evolution of the other dependent variables in this article—including z, δ, and χ. We consider its two-time autocorrelation function and its frequency spectrum. Figure 13 shows the autocorrelation functions of $a(t)$, $\rho(a; \tau)$, at R_λ 38 and 93, for a small time lag range—up to 10 Kolmogorov scales. Like most one-time statistics considered so far, the Reynolds-number dependence is small and may not be statistically significant. It is seen that $\rho(a; \tau)$ falls rapidly near the origin, being only

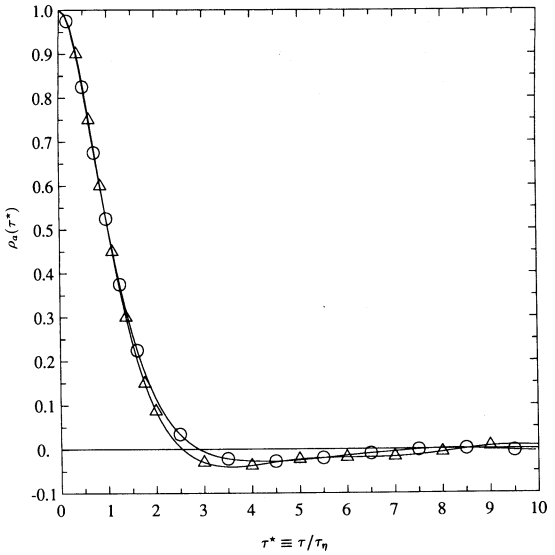

Fig. 13. Autocorrelation function $\rho_a(\tau^*)$ of surface strain time series $a^*(t^*)$, at R_λ 38 (Δ) and R_λ 93 ($\bigcirc$). Time lag τ is normalized by τ_η.

about 0.1 at $\tau \approx 2\tau_\eta$, and crosses the zero line at $\tau \approx 3\tau_\eta$ to sustain a small negative loop.

The integral time scale of $a(t)$, T_a, is about 1 Kolmogorov time scale for all Reynolds numbers ($0.96\tau_\eta$ at R_λ 38, and $1.03\tau_\eta$ at R_λ 93). By contrast, the integral time scale of $\chi_0(t)$ is about $4\tau_\eta$.

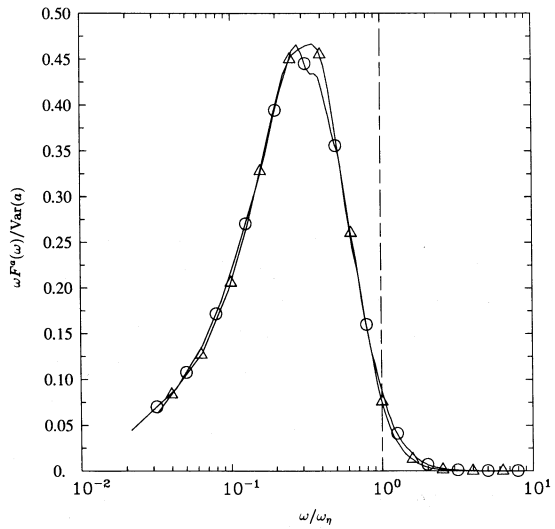

Fig. 14. Normalized frequency spectrum of surface strain time series $a^*(t^*)$, at R_λ 38 (Δ) and R_λ 93 ($\bigcirc$). Frequency (ω) is scaled by the Kolmogorov frequency $\omega_\eta \equiv \pi/\tau_\eta$: vertical dashed line is at $\omega = \omega_\eta$.

To study the frequency content of $a(t)$, in Fig. 14 we examine its normalized frequency spectra $F^a(\omega)$ at R_λ 38 and 93 (which are Fourier transforms of the autocorrelations). At any frequency ω, the ordinate of each curve is proportional to the contributions from an infinitesimal frequency band centered (logarithmically) on ω. Evidently, $F^a(\omega)$ has an appreciable, though small, contribution from frequencies higher than the Kolmogorov frequency $\omega_\eta (\equiv \pi/\tau_\eta)$. The peak range is associated with time scales of order $3\tau_\eta$.

5. PRINCIPAL STRAINS IN THE TANGENT PLANE

5.1 Statistics of S_1 and S_2

We now examine the nature of the straining in the tangent plane of a material surface, through the principal strain rates S_1 and S_2 (defined in Sec. 2.2), normalized by the Kolmogorov time scale ($S_1^* \equiv S_1\tau_\eta$, $S_2^* \equiv S_2\tau_\eta$). The means and standard deviations of S_1^* and S_2^*, all area-weighted, are given in Table 4. It may be seen that, on average, S_1 is extensive, but S_2 is (very slightly) compressive. The mean values of S_1^* and S_2^* are approximately 0.315 and -0.035, respectively, with magnitudes decreasing slightly with Reynolds number. The sum of $\langle S_1^* \rangle$ and $\langle S_2^* \rangle$ is, of course, the mean nondimensional surface strain, $\langle a^* \rangle$. The standard deviations of both are less than that of a^* ($\approx$0.34, from Table 2). Surface elements of large areas result from strong stretching (with large a), which implies a large S_1 (and possibly S_2). The effect of area-weighting on the statistics considered in this section is thus to increase the contributions from large S_1 and S_2 values.

The joint pdf of S_1^* and S_2^* contains complete one-point statistical information, from which all moments can be derived. A contour plot obtained from the R_λ 93 simulation is shown in Fig. 15. Since by definition $S_1 \geq S_2$, the isoprobability contours are necessarily restricted to the right of the diagonal line drawn through the origin. The shape and location of these contours indicate that S_1 is almost always positive, and that there is relatively high probability of S_2 taking values of small magnitude. The global maximum of the

TABLE 4

Moments of Surface Strain Components (Area-Weighted)

R_λ	38	63	90	93
$\langle S_1^* \rangle_A$	0.324	0.312	0.306	0.315
$\langle S_2^* \rangle_A$	−0.037	−0.038	−0.033	−0.032
σ_A of S_1^*	0.169	0.172	0.178	0.176
σ_A of S_2^*	0.239	0.240	0.232	0.232
P_A	0.478	0.481	0.487	0.498
P_B	0.208	0.203	0.205	0.201
P_C	0.118	0.113	0.112	0.110
P_D	0.107	0.107	0.106	0.100
P_E	0.075	0.081	0.076	0.077
P_F	0.012	0.014	0.013	0.014
$P(S_1 > S_2 > S_N)$	0.687	0.685	0.692	0.698

joint pdf occurs at approximately the coordinates $S_1^* = 0.3$, $S_2^* = 0.05$.

The strain S_N normal to the surface is known at each point in the S_1–S_2 plane (related by continuity: $S_N = -S_1 - S_2$). It is useful to recognize that the sample space of S_1 and S_2 can be partitioned into six mutually exclusive events, or, equivalently, distinct regions of the S_1–S_2 plane. Each such event represents a specific algebraic ordering of S_1, S_2, S_N, and zero, delineated as follows:

$$\begin{aligned}
&\text{A:} \quad S_1 \geq S_2 \geq 0 \geq S_N, \\
&\text{B:} \quad S_1 \geq 0 \geq S_2 \geq S_N, \\
&\text{C:} \quad S_1 \geq 0 \geq S_N > S_2, \\
&\text{D:} \quad S_1 \geq S_N \geq 0 \geq S_2, \\
&\text{E:} \quad S_N > S_1 \geq 0 \geq S_2, \\
&\text{F:} \quad S_N \geq 0 \geq S_1 \geq S_2.
\end{aligned} \tag{48}$$

The regions corresponding to these events are marked in Fig. 15 after simplifying the inequalities to

$$\begin{aligned}
&\text{A:} \quad S_2 \geq 0, \\
&\text{B:} \quad 0 > S_2 \geq -\frac{1}{2} S_1, \\
&\text{C:} \quad -\frac{1}{2} S_1 > S_2 \geq -S_1, \\
&\text{D:} \quad -S_1 > S_2 \geq -2S_1, \\
&\text{E:} \quad S_2 < -2S_1 \geq 0, \\
&\text{F:} \quad S_1 < 0.
\end{aligned} \tag{49}$$

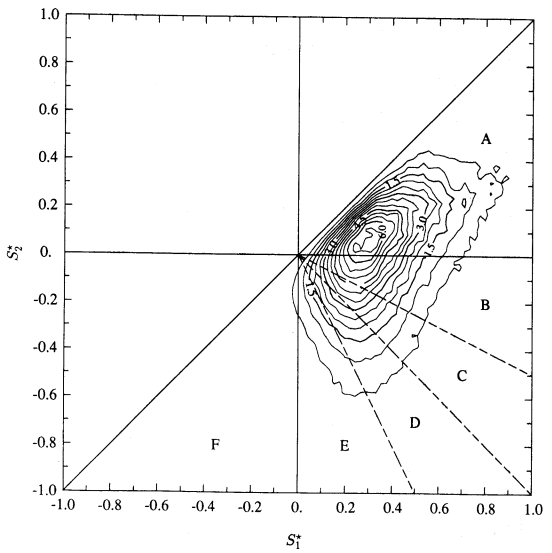

Fig. 15. Contour plot of (area-weighted) joint pdf of Kolmogorov-scaled principal surface strain components S_1^* and S_2^*, from R_λ 93 data. Contour levels are shown multiplied by 10. Contour interval is 0.05. Boundaries between the six regions A to F (Sec. 5.1) are as indicated.

Their probabilities, denoted by $P_A \cdots P_F$ (the sum is unity), are given in Table 4. All are seen to be effectively independent of Reynolds number.

The net strain in the tangent plane, i.e., $a(t)$ ($\equiv S_1 + S_2$), is compressive under events D, E, and F. The case of strong compressive straining with S_1 and S_2 both negative occurs only as event F, which is rare, with less than 2% probability (area-weighted). The data also show that S_2 is compressive over nearly half of the surface area. The most probable ordering among S_1, S_2, and S_N is that of $S_1 > S_2 > S_N$. Its probability is the sum of P_A and P_B, about 69% (but only 55% without area-weighting).

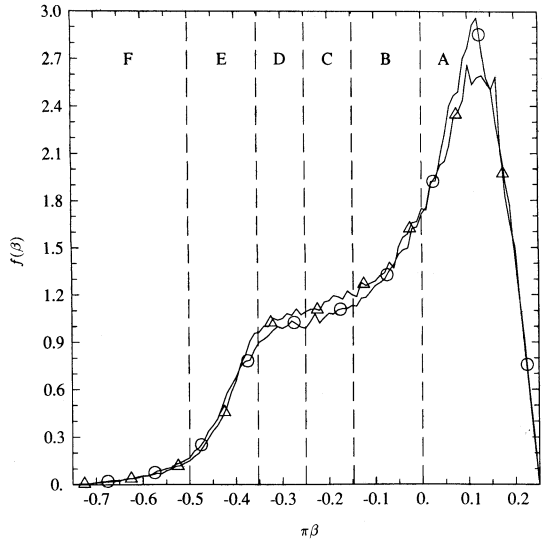

Fig. 16. Probability density (area-weighted) of angle β (Eq. 50) in S_1–S_2 plane, at R_λ 38 (Δ) and R_λ 93 ($\circ$). The angle is multiplied by π. Boundaries between the six regions A to F (Sec. 5.1) are as indicated.

Directional preferences, if any, of the tangent-plane straining are described by the angular orientation of (S_1, S_2) vector. Let β be the angle in the S_1–S_2 plane, measured from the S_1 axis:

$$\beta = \arccos(S_1/\sqrt{S_1^2 + S_2^2}). \tag{50}$$

Because $S_1 > S_2$, β it must lie between $-3\pi/4$ and $\pi/4$. Figure 16 shows its pdf, for the R_λ 38 and 93 simulations. A high peak is observed, near 0.10π, becoming more prominent at higher Reynolds numbers. The pdfs are nearly flat between 0.15π and 0.35π. Also, the pdfs vanish at both ends. Boundaries between the six regimes A–F are shown as dashed lines. The (unconditional) pdf of β is equal to a weighted sum of the conditional pdfs under each regime, with $P_A \cdots P_F$ as the weighting factors. From Fig. 16 it is evident that these conditional pdfs differ greatly in character.

5.2 Comparison with Principal Strains

The distribution of the strain-rate components S_1, S_2, and S_N is now briefly compared with that of the principal strain rates (denoted by $\Lambda_1, \Lambda_2, \Lambda_3$) obtained from the three-dimensional strain-rate tensor. Ashurst et al. [33] have recently obtained numerical results by analyzing data from direct simulations. Two cases were studied: the isotropic turbulence simulations made by Kerr [30] and the shear flow simulations by Rogers and Moin [34], and were found to give similar results. Despite a difference in approach (Lagrangian versus Eulerian), a comparison between our results and theirs is legitimate because the one-point one-time Eulerian and Lagrangian pdfs are the same in homogeneous incompressible turbulence.

We use the conventional ordering $\Lambda_1 \geq \Lambda_2 \geq \Lambda_3$. Our results are virtually Reynolds-number independent when normalized by the Kolmogorov scales. Because there is no direct connection between the principal strains evaluated at a material point and the area of the surface element on which the point lies, area-weighting is *not* used on the statistics of Λ_1, Λ_2, and Λ_3. The results indicate two extensive princpal directions in the mean state of straining, with the Kolmogorov-scaled mean values of Λ_1, Λ_2, and Λ_3 being 0.39, 0.09, and -0.48, respectively.

The intermediate strain Λ_2 is given the most attention. We normalize it by the strain-rate amplitude e ($e^2 \equiv \Lambda_1^2 + \Lambda_2^2 + \Lambda_3^2$) such that $\hat{\Lambda}_2 \equiv \sqrt{6}\Lambda_2/e$ lies between ± 1. The pdf of $\hat{\Lambda}_2$ is shown in Fig. 17 for the R_λ 38 and 93 simulations. The shape of this pdf is similar to that described by Ashurst et al. [33]. In particular, this pdf is observed to vanish at the limiting values -1 and 1, which correspond to $\Lambda_2 = \Lambda_3$ and $\Lambda_2 = \Lambda_1$, respectively.

By virtue of the continuity condition $\Lambda_1 + \Lambda_2 + \Lambda_3 = 0$, each value of $\hat{\Lambda}_2$ corresponds to an unique strain-rate ratio $\Lambda_1 : \Lambda_2 : \Lambda_3$. The most probable value of this ratio, indicated by the peak location of the pdf, is approximately 0.55, corresponding to $\Lambda_1 : \Lambda_2 : \Lambda_3 = 2.53 : 1 : -3.53$. Ashurst et al. reported the mean value given $\Lambda_2 > 0$ to be $3 : 1 : -4$ (to one significant figure). From our data, this mean ratio is $3.25 : 1 : -4.25$ (at $\hat{\Lambda}_2 = 0.45$). A fairly close agreement is thus observed.

As with Λ_2, we normalize the smaller strain S_2 in the tangent plane to give $\hat{S}_2 \equiv \sqrt{6}S_2/s^2$, where $s^2 \equiv S_1^2 + S_2^2 + S_N^2$. But the limiting values of $\hat{S}_2$ are different from those of Λ_2. It may

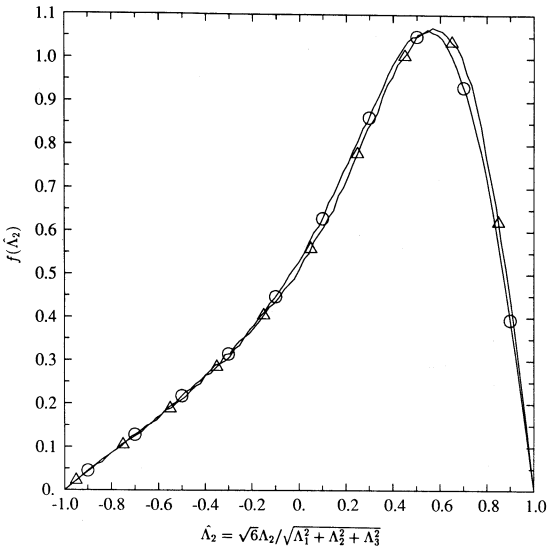

Fig. 17. Probability density of normalized intermediate principal strain $\hat{\Lambda}_2$ (Sec. 5.2) (from the strain-rate tensor **S**), at R_λ 38 (Δ) and R_λ 93 ($\circ$).

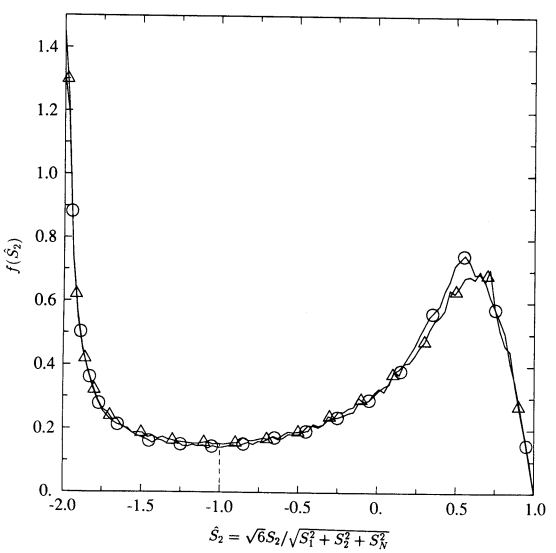

Fig. 18. Probability density of normalized smaller component $\hat{S}_2$ (Sec. 5.2) of principal strain in the tangent plane, at R_λ 38 (Δ) and R_λ 93 ($\circ$). (Note that the range is different from that of $\hat{\Lambda}_2$ shown in Fig. 17).

be readily shown that S_2 lies between ± 1 only when $S_1 \geq S_2 \geq S_N$—which is analogous to the principal-strain ordering $\Lambda_1 \geq \Lambda_2 \geq \Lambda_3$. We recall from Sec. 5.1 this ordering occurs with about 69% probability. In the rest of the surface strain configurations $\hat{S}_2$ lies between -2 and -1.

Figure 18 shows the pdf of $\hat{S}_2$ at R_λ 39 and 93. There is no clear dependence on Reynolds number. The probability of $\hat{S}_2$ lying near its lower limit at -2 (which gives $S_1 : S_2 : S_N = 1 : -2 : 1$, with S_2 negative) is evidently high. However the pdf also drops sharply in that region. The part of broad local maximum occurs near $\hat{S}_2 = 0.5$, the location of the global maximum in the pdf of $\hat{\Lambda}_2$.

6. SUMMARY AND CONCLUSIONS

The results reported in this article have been obtained from Direct Numerical Simulations of constant-density, stationary, homogeneous, isotropic turbulence with Taylor-scale Reynolds numbers (R_λ) in the range 38–93. When normalized by the Kolmogorov scales, none of the surface-property statistics examined displays a significant Reynolds-number dependence. This is in contrast to the findings of Yeung and Pope [23] for acceleration and velocity-gradient statistics.

In each simulation an ensemble of 4096 infinitesimal material surface elements is tracked to determine, primarily, the time series of strain-rate acting on each surface element. From these time series the other statistics required are deduced.

In the flamelet regime, a premixed flame can be modeled as a surface propagating (relative to the fluid) at the local laminar flame speed w. If w/v_η (with v_η denoting the Kolmogorov velocity scale) is not too large, the propagating surface (i.e., the flamelet) remains close to an initially coincident material surface. Specifically, the distance z between the surfaces is

$$z = \mathcal{L} + \eta(w_0/v_\eta)Z \tag{51}$$

(see Eq. 27). The dependence of w on the strain rate (see Eq. 23) increases z by precisely the Markstein length, $\mathcal{L}$. In the stationary state, the mean of the stochastic process Z is about 4.0, and, with probability 0.8, Z is less than 5.0 (Table 1).

In many experiments and applications w is significantly greater than v_η. Indeed, simple scaling arguments yield

$$w/v_\eta \approx (\delta_L/\eta)^{-1}, \tag{52}$$

where δ_L is the laminar flame thickness. Thus, if the combustion is well within the flamelet regime (i.e., $(\delta_L/\eta \ll 1)$, then w/v_η must be large. In this case the analysis used here is no longer valid.

For small and large values of w/v_η, the rate-of-strain acting on a premixed flamelet is well approximated by a and α, respectively. These are the rate-of-strain on a material surface (a) and that on a randomly-oriented surface (α). The statistical properties of a and α are summarized in Table 2. Although the mean of α is zero, that of a (i.e., $\langle a \rangle_A$), is about $0.28/\tau_\eta$ (with τ_η denoting the Kolmogorov time scale)—about 80% of its standard deviation. The probability of compressive straining is 0.53 for α and 0.20 for a.

One significance of the steady-state value of $\langle a \rangle_A$ is that its inverse is the time scale of the exponential growth of area of a material surface element:

$$\frac{d \ln\langle A \rangle}{dt} = \langle a \rangle_A. \tag{53}$$

Thus the average time taken for the area to double is $\ln 2/\langle a \rangle_A \approx 2.5\tau_\eta$.

To address questions related to turbulent diffusion flames in the flamelet regime, we have examined the statistics of diffusive layers centered on a material surface. Subject to three assumptions (stated after Eq. 35 in Sec. 4.1), the diffusive layer thickness is given by

$$\delta = \eta\delta^* \mathrm{Sc}^{-1/2} \tag{54}$$

(see Eq. 39). The pdf of the nondimensional random variable δ^* is shown in Fig. 9 (for the stationary case). There is only 2% probability of δ^* exceeding 5.

For liquid flows—sometimes used in analogues of diffusion flames—it is clear that δ is almost certainly small compared to η, since the Schmidt number is large. For gaseous flows $(\mathrm{Sc} \approx 1)\,\delta$ is comparable to η.

The scalar dissipation at the center of the diffusive layer, χ_0, is found to be (to a fair approximation) log-normally distributed. But the variance of $\ln \chi_0$ (about 0.7) is about one third of that of $\ln \epsilon_\phi$, where ϵ_ϕ is the scalar dissipation for a conserved passive scalar. It has been shown that the difference can be eliminated by sampling χ throughout the diffusive layer, and by allowing for random concentration differences across the layer.

Flamelet theories assume—among other things—that the flame structure responds instantly to changes in the scalar dissipation. This assumption could be tested by performing transient one-dimensional laminar flame calculations with a prescribed stochastic strain-rate time series, to simulate the strain rate (and hence scalar dissipation) experienced by a turbulent flamelet. To aid such a study, the strain-rate time series has been characterized. In particular, it is found that the integral time scales of $a(t)$ and $\chi_0(t)$ are about τ_η and $4\tau_\eta$, respectively.

In the tangent plane of a material surface element there is a two-dimensional strain-rate tensor, with principal values S_1 and S_2 $(S_1 \geq S_2)$. Studies (experimental or theoretical) of laminar flames (premixed or diffusion) usually assume either axisymmetric strain $(S_1 = S_2 > 0)$ or plane strain $(S_1 > 0, S_2 = 0)$. For a material surface in isotropic turbulence, the joint statistics of S_1 and S_2 have been determined (see, e.g., Table 4). Although S_1 is almost always positive (with 98.5% probability), S_2 has about equal probability of being positive or negative. The most likely ordering of the strain rates (about 70% probability) is $S_1 > S_2 > S_N$ (where $S_N = -a$ is the strain normal to the surface).

The distribution of the principal strains (ordered as $\Lambda_1 \geq \Lambda_2 \geq \Lambda_3$) obtained from the full three-dimensional strain-rate tensor have also been studied. Characteristic features such as the most probable value of the ratio $\Lambda_1 : \Lambda_2 : \Lambda_3$ are in good agreement with the numerical results of Ashurst et al. [33]. The intermediate principal strain Λ_2 is extensive in the mean. Its pdf is very different from that of S_2 considered above, even when the latter is conditioned on the analogous ordering $S_1 > S_2 > S_N$ (Figs. 17 and 18).

Finally, it is emphasized that area-weighting is appropriate to surface statistics. The difference between weighted and unweighted values can be large. For example, the area-weighted mean of the normalized distance Z is less than half of the unweighted mean; this is true for the variance of $\ln \chi_0$ as well.

The direct determination of area-weighted means results in large statistical errors at large times. A method to overcome this difficulty for stationary statistics is presented in Appendix B.

This article has provided an example of the successful use of Lagrangian time series to answer important physical questions. As described by Yeung [36], this approach offers many other possibilities. In a separate paper [37], we study the curvature of material surfaces in isotropic turbulence.

This work was supported by the U.S. Air Force Office of Scientific Research (grant number AFOSR-88-0052). Computations conducted during the research were performed on the Cornell National Supercomputer Facility, which is supported in part by the National Science Foundation, New York State, the IBM Corporation and the members of the Corporate Research Institute.

REFERENCES

1. Peters, N., *Twenty-First Symposium (International) on Combustion*, The Combustion Institute, Pittsburgh, 1986, p. 1231.
2. Monin, A. S., and Yaglom, A. M., in *Statistical Fluid Mechanics*. (J. L. Lumley, Ed.), MIT Press, Cambridge, MA, 1975, vol. 2.
3. Bray, K. N. C., in *Turbulent Reacting Flows* (P. A. Libby and F. A. Williams, Eds.), Springer, Berlin, 1980, p. 115.
4. Pope, S. B., *Annu. Rev. Fluid Mech.* 19:237–270 (1987).
5. Abraham, J., Williams, F. A., and Bracco, F. V., *SAE Pap.* 850345 (1985).
6. Pope, S. B., *Int. J. Eng. Sci.* 26:445–470 (1988).
7. Law, C. K., Zhu, D. L., and Yu, G., Propagation and extinction of stretched premixed flames. *Twenty-First Symposium (International) on Combustion*, The Combustion Institute, Pittsburgh, 1986, p. 1419.
8. Abdel-Gayed, R. G., Bradley, D., and Lau, A. K. C., *Twenty-Second Symposium (International) on Combustion*, The Combustion Institute, Pittsburgh, 1988, p. 731.
9. Cant, R. S., and Bray, K. N. C., *Twenty-Second Symposium (International) on Combustion*, The Combustion Institute, Pittsburgh, 1988, p. 791.
10. Pope, S. B., and Cheng, W. K., *Twenty-Second Symposium (International) on Combustion*, The Combustion Institute, Pittsburgh, 1988, p. 781.
11. Bilger, R. W., in *Turbulent Reacting Flows* (P. A. Libby and F. A. Williams, Eds.), Springer, Berlin, 1980, p. 65.
12. Bilger, R. W., *Annu. Rev. Fluid Mech.* 21:101–135 (1989).
13. Burke, S. P., and Schumann, T. E. W., *Ind. Eng. Chem.* 20:998–1004 (1928).
14. Williams, F. A., in *Turbulent Mixing in Nonreactive and Reactive Flows* (S. N. B. Murthy, Ed.), Plenum, New York, 1975, p. 189.
15. Liew, S. K., Bray, K. N. C., and Moss, J. B., *Combust. Sci. Technol.* 27:69–73 (1981).
16. Liew, S. K., Bray, K. N. C., and Moss, J. B., *Combust. Flame* 56:199–213 (1984).
17. Peters, N., *Prog. Ener. Combust. Sci.* 10:319–339 (1984).
18. Bilger, R. W., *Twenty-Second Symposium (International) on Combustion* (invited plenary lecture), The Combustion Institute, Pittsburgh, 1988, p. 475.
19. Mitchell, R. E., Sarofim, A. F., and Clomburg, L. A., *Combust. Flame* 37:227–244 (1980).
20. Smooke, M. D., Seshadri, K., and Puri, I. K., *Twenty-Second Symposium (International) on Combustion*, The Combustion Institute, Pittsburgh, 1988, p. 1555.
21. Williams, F. A., *Combustion Theory*, 2nd ed., Benjamin-Cummings, Menlo Park, CA, 1985.
22. Rogg, B., Behrendt, F., and Warnatz, J. *Twenty-First Symposium (International) on Combustion*, The Combustion Institute, Pittsburgh, 1986, p. 1533.
23. Yeung, P. K., and Pope, S. B., Lagrangian statistics from direct numerical simulations of isotropic turbulence. *J. Fluid Mech.* 207:531–586 (1989).
24. Eswaran, V., and Pope, S. B., *Comput. Fluids* 16:257–278 (1988).
25. Rogallo, R. S., *Numerical Experiments in Homogeneous Turbulence*, NASA Tech. Memo, 81315 (1981).
26. Yeung, P. K., and Pope, S. B., *J. Comput. Phys.* 79:373–416, 1988.
27. Matalon, M., and Matkowsky, B. J., *J. Fluid Mech.* 124:239–259 (1982).
28. Markstein, G. M., *Non-Steady Flame Propagation*, Macmillan, New York, 1964.
29. Hinze, J. O., *Turbulence*, 2nd ed., McGraw-Hill, New York, 1975.
30. Kerr, R. M., *J. Fluid Mech.* 153:31–58 (1985).
31. Law, C. K., Ishizuka, S., and Cho, P., *Combust. Sci. Technol.* 28:89–96 (1982).
32. Eswaran, V., and Pope S. B., *Phys. Fluids* 31:506–520 (1988).
33. Ashurst, W. T., Kerstein, A. R., Kerr, R M., and Gibson, C. H., *Phys. Fluids* 30:2343–2353 (1987).
34. Rogers, M. M., and Moin, P., *J. Fluid Mech.* 176:33–66 (1987).
35. Batchelor, G. K., *An Introduction to Fluid Dynamics*, Cambridge University Press, Cambridge, 1967.
36. Yeung, P. K., PhD thesis, Cornell University, 1989.
37. Pope, S. B., Yeung, P. K., and Girimaji, S. S., Phys. Fluids A 1:2010–2018 (1989).

Received 28 October 1988; revised 6 April 1989

APPENDIX A: CALCULATION OF STRAIN COMPONENTS (S_1, S_2, S_N)

A comprehensive account of the geometry of material surfaces has been provided by Pope [6]. Here we consider only those aspects essential to the present problem.

The crucial step is the determination of the unit normal $\mathbf{N}(t)$ at a given point on the material surface, whose tangent plane is spanned by two linearly independent material line vectors $\mathbf{s}^{(1)}(t)$ and $\mathbf{s}^{(2)}(t)$. The analysis thus begins with the equation for material line element deformation. Let $\mathbf{s}(t)$ be an infinitesimal material vector at time t, and $\mathbf{r}$ be its initial value $\mathbf{s}(0)$. The rate of change of $\mathbf{s}(t)$ is given by (e.g., [35])[4]

$$\dot{\mathbf{s}} = G\mathbf{s}, \tag{A1}$$

where $\mathbf{G}(t)$ is the instantaneous velocity gradient tensor (i.e., $G_{ij} \equiv \partial u_i/\partial x_j$) following the fluid particle. As in Ref. 2, we express $\mathbf{s}$ in terms of $\mathbf{r}$ by

$$\mathbf{s} = \mathbf{B}\mathbf{r}, \tag{A2}$$

where the matrix $\mathbf{B}(t)$ evolves by

$$\dot{\mathbf{B}} = \mathbf{G}\mathbf{B}, \tag{A3}$$

with $\mathbf{B}(0)$ being the identity matrix. Equation A3 is integrated numerically by a fourth-order Runge–Kutta method.

The above equations are used to determine $\mathbf{s}^{(1)}(t)$ and $\mathbf{s}^{(2)}(t)$. In view of the isotropy of the turbulence, the initial values $\mathbf{s}^{(1)}(0)$ and $\mathbf{s}^{(2)}(0)$ are arbitrary: we specify them respectively as the unit vectors $\mathbf{e}_1 \equiv (1, 0, 0)$ and $\mathbf{e}_2 \equiv (0, 1, 0)$ in a fixed Cartesian coordinate system $\mathbf{x}$. Once $\mathbf{s}^{(1)}(t)$ and $\mathbf{s}^{(2)}(t)$ are determined, Eqs. 5 and 8 are used to calculate the area amplification factor $A(t)$, and hence the normal $\mathbf{N}(t)$.

For each material element we introduce a moving and rotating Cartesian coordinate system $\mathbf{x}'$ (with unit vectors $\mathbf{e}'_1$, $\mathbf{e}'_2$, $\mathbf{e}'_3$) such that $\mathbf{N}(t)$ is coincident with $\mathbf{e}'_3$. This is achieved by a rotation of the original (fixed) frame, defined by an orthogonal matrix $\mathbf{Q}$, such that

$$\mathbf{e}'_i = Q_{ij}\mathbf{e}_j. \tag{A4}$$

The required elements of $\mathbf{Q}$ are

$$\mathbf{Q} = \begin{bmatrix} \cos\theta & \sin\theta & 0 \\ -\sin\theta\cos\phi & \cos\theta\cos\phi & \sin\phi \\ \sin\theta\sin\phi & -\cos\theta\sin\phi & \cos\phi \end{bmatrix}, \tag{A5}$$

where, with N_1, N_2, N_3 denoting the components of $\mathbf{N}(t)$,

$$\cos\phi = N_3$$

$$\sin\phi = \sqrt{N_1{}^2 + N_2{}^2},$$

$$\cos\theta = -N_2/\sqrt{N_2{}^1 + N_2{}^2},$$

$$\sin\theta = N_1/\sqrt{N_2{}^1 + N_2{}^2}. \tag{A6}$$

The formulation is completed by transforming the strain-rate tensor $\mathbf{S}$ as a second-order tensor. The components of $\mathbf{S}$ in the new Cartesian frame $\mathbf{x}'$, denoted by $\mathbf{S}'$, are given by[5]

$$\mathbf{S}' = \mathbf{Q}\mathbf{S}\mathbf{Q}^T. \tag{A7}$$

In particular, the strain normal to the surface is

$$S_N = S'_{33} = \mathbf{N}^T\mathbf{S}\mathbf{N} = S_{ij}N_iN_j. \tag{A8}$$

All elements of $\mathbf{S}'$ are generally nonzero, unless $\mathbf{N}(t)$ happens to be an eigenvector of $\mathbf{S}$, in which case $\mathbf{S}'$ would be diagonal.

Straining in the tangent plane is described by the submatrix

$$\tilde{\mathbf{S}} = \begin{vmatrix} S'_{11} & S'_{12} \\ S'_{21} & S'_{22} \end{vmatrix}. \tag{A9}$$

The eigenvalues of $\tilde{\mathbf{S}}$ are defined to be S_1 and S_2, with the convention $S_1 \geq S_2$.

[4] Overdots indicate time derivatives.

[5] Superscript T stands for vector or matrix transpose.

APPENDIX B: CALCULATION OF AREA-WEIGHTED STATISTICS

As stated in Sec. 2.3, the direct use of Eqs. 13 and 14 to calculate area-weighted averages at large time can result in large statistical errors. This is attributed to the fact, shown below, that the variance of the surface element area $A(t)$, and hence the weighting factor, increase rapidly—approximately exponentially—with time.

We begin by integrating Eq. 7 for the area amplification factor $A(t)$ to obtain

$$\ln A(t) = \int_0^t a(s)\, ds \tag{B1}$$

(since $A(0) = 1$). Assuming that the time series $a(t)$ is stationary and its integral time scale T_a is finite (as well justified by numerical evidence), then application of the central limit theorem for integrals to this equation indicates that, for $t \gg T_a$, $\ln A(t)$ is normally distributed—regardless of the distribution of a. Specifically, under such conditions,

$$\ln A(t) \overset{D}{=} \mathfrak{N}[\langle a\rangle t,\ 2\,\mathrm{var}(a) T_a t]. \tag{B2}$$

(The notation $X \overset{D}{=} \mathfrak{N}[\mu, \sigma^2]$ indicates that the random variable X is normally distributed with mean μ and variance σ^2.) Hence, from Eq. 14 and using the properties of a log-normal distribution,

$$\ln w = \ln\left(A(t)/\langle A(t)\rangle\right) \overset{D}{=} \mathfrak{N}[-\mathrm{var}\,(a) T_a t,\ 2\mathrm{var}\,(a) T_a t], \tag{B3}$$

from which the variance of the area-weights can be readily shown to be

$$\mathrm{var}(w) = \exp(2\mathrm{var}(a) T_a t) - 1. \tag{B4}$$

Substituting typical values of var(a) (unweighted) and T_a from Table 2 and Sec. 4.2, we find var(w) to be about 5 at $t = 10\tau_\eta$, and as high as 35 at $t = 20\tau_\eta$.

If the surface strain a is close to Gaussian, the above statements on the log-normality of the surface area distribution are also valid at times not necessarily large compared to T_a. The standardized pdf of $\ln A$ is then independent of time, and may be expected to be also close to Gaussian. Figure 19, which shows this standardized pdf at R_λ 38 and 93, confirms this. It may be seen that large values are more probable than in a Gaussian distribution—this pdf has a *positive* skewness coefficient of 0.35. In other words, the area is more intermittent than a log-normal random variable.

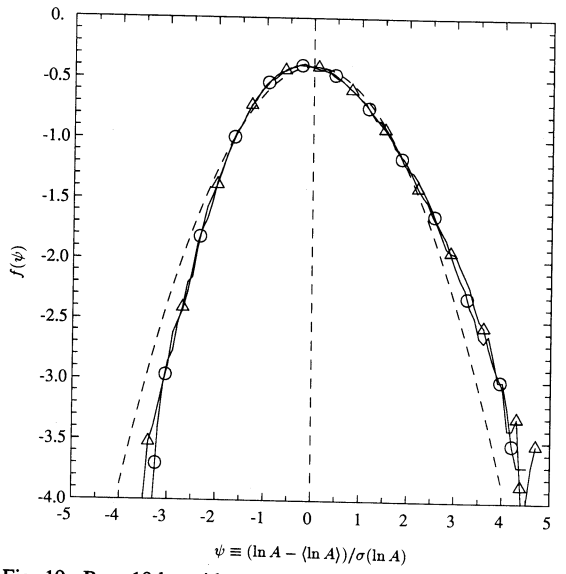

Fig. 19. Base-10 logarithm of the standardized pdf of the logarithm of surface element area, at R_λ 38 (Δ) and R_λ 93 (○). Skewness coefficients (μ_3) are 0.35 and 0.34, respectively; the flatness factors (μ_4) are 3.23 and 3.14. Dashed line (parabola) represents standard Gaussian density.

From the above it is clear that, especially at large times, sporadic occurrences of extremely large surface areas (and large weights) lead to unacceptably large statistical errors in the estimation of area-weighted means. Indeed, at $t = 20\tau_\eta$, a few surface elements of area of order 500 times the average value—resulting in a spiky area-weighted pdf—have been found in the calculations. To obtain reliable area-weighted statistics, at large times, a means of reducing the statistical error is necessary.

In the case of dynamically developing quantities for which initial conditions have an intrinsic significance, no remedial treatment has been devised. Thus, for instance, statistics of the growing separation distance $z(t)$ between a propagating surface and an initially coincident material sur-

face are subject to considerable statistical errors at large times ($t > 12\tau_\eta$, say). The curves in Fig. 5 clearly become more irregular as time increases.

However, for quantities that attain a stationary distribution, a strategy to reduce the statistical errors is available, as described and justified below. Fortunately, most surface properties considered in this article (a, χ, and δ) belong to this latter class.

Consider $\langle\phi(t)\rangle_A$—the area-weighted mean of $\phi(t)$, starting from initial conditions at $t = 0$ (as before, $A(0) = 1$). If the single-time area-weighted statistics of $\phi(t)$ become stationary, then after some time t_s, $\langle\phi(t)\rangle_A$ is acceptably close to its stationary value $\langle\phi\rangle_A$. Then, from a time series of length T, the standard way to estimate $\langle\phi\rangle_A$ is to form the time average of (the estimate of) $\langle\phi(t)\rangle_A$ between $t = t_s$ and $t = T$. (By assumption T is greater than t_s, for otherwise $\langle\phi\rangle_A$ cannot be estimated.)

As mentioned above, the problem with this straightforward approach is that the statistical error increases exponentially with time: at $t = T$ it may be much larger than at $t = t_s$. A way to reduce the statistical error is, for each $t(t_s \le t \le T)$, to reinitialize the amplification factors to unity at time $t - t_s$. In other words, at any $t \ge t_s$, the age of the surface (i.e., the time since (re)-initialization) is t_s—the earliest time at which stationarity is observed.

The method outlined above is implemented efficiently through the observation that the ratio $A(t)/A(t - t_s)$ is the amplification factor since the time $t - t_s$. In the following we use a general time t' instead of t_s, in order to investigate the dependence of area-weighted statistics on the choice of t'. Thus, the method amounts to replacing the weight of each element (Eq. 14) by

$$w_i' = \frac{A_i(t)/A_i(t - t')}{\langle A_i(t)/A_i(t - t')\rangle}. \tag{B5}$$

Note that $t' = 0$ corresponds to equal weighting, and $t' = t$ reduces to Eq. 14 (i.e., regular area-weighting). We next consider how a suitable choice of t' can be chosen to produce accurate area-weighted averages without large statistical error.

With the aid of Eq. B1, the exact area-weighted mean of a material surface property ϕ, as defined by Eq. 12, can be written as

$$\langle\phi(t)\rangle_A = \frac{\left\langle \phi(t) \exp \int_0^t a(s)\, ds \right\rangle}{\left\langle \exp \int_0^t a(s)\, ds \right\rangle}. \tag{B6}$$

Let $A^*(t_1, t_2)$ be the area amplification between t_1 and $t_2 > t_1$:

$$A^*(t_1, t_2) = \exp\left\{ \int_{t_1}^{t_2} a(s)\, ds \right\} = A(t_2)/A(t_1). \tag{B7}$$

If the time interval $[0, t]$ is broken into $[0, t - t']$ and $[t - t', t]$, Eq. B6 becomes

$$\langle\phi(t)\rangle_A = \frac{\langle\phi(t)A^*(0, t - t')A^*(t - t', t)\rangle}{\langle A^*(0, t - t')A^*(t - t', t)\rangle}. \tag{B8}$$

For $t' \gg T_\phi$ (the integral time scale of $\phi(t)$, assumed finite and non-zero), $\phi(t)$ is uncorrelated with $A^*(0, t - t')$. If we further *assume* the correlation between $A^*(0, t - t')$ and $A^*(t - t', t)$ (over adjacent but separate time intervals) to be weak, then $\langle A^*(0, t - t')\rangle$ can be factorized out of both the numerator and denominator. We thus arrive at

$$\langle\phi\rangle_A \approx \frac{\langle\phi(t)A^*(t - t', t)\rangle}{\langle A^*(t - t', t)\rangle} = \frac{\langle\phi(t)A(t)/A(t - t')\rangle}{\langle A(t)/A(t - t')\rangle}. \tag{B9}$$

This final form agrees exactly with the substitution of the new weights (Eq. B5) in place of w_i in Eq. 13. It appears that a necessary condition for the weak correlation between $A^*(0, t - t')$ and $A^*(t - t', t)$ is $t' \gg T_a$ (the integral time scale of $a(t)$). These considerations suggest that the age of the surface t' should be chosen to be greater than both T_a and T_ϕ.

Since Kolmogorov scaling is found to remove the Reynolds-number dependence in the results of this article, and $T_a \approx \tau_\eta$, the time lapse t' is best expressed in Kolmogorov scales. Because of the

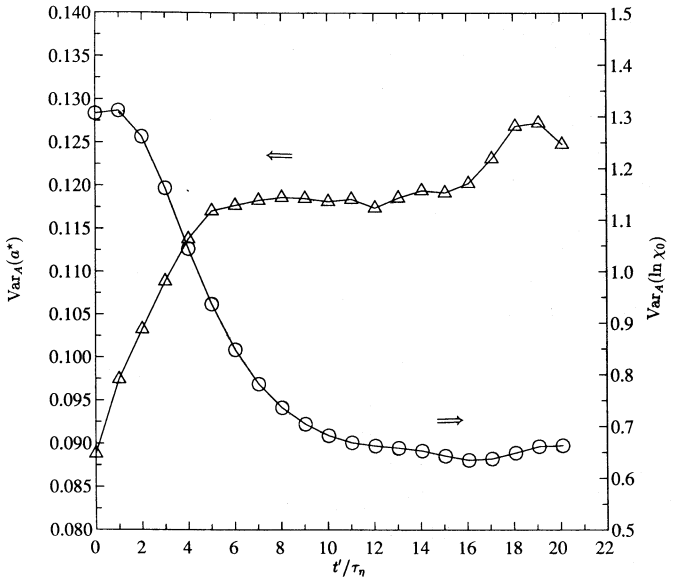

Fig. 20. Effect of time-lapse t' on area-weighting of the variances of a^* (△) and $\ln \chi_0^*$ (○) (note the different scales used). The data are obtained from a R_λ 54 simulation performed by Yeung and Pope [23].

requirement $t' \gg T_\phi$, the proper value of t'/τ_η can be expected to be different for each variable ϕ. The choice is made in an empirical manner, by studying the effect of various values of t'/τ_η. It needs to be demonstrated that as t'/τ_η increases, the statistic calculated reaches a plateau corresponding to $\langle\phi\rangle_A$ before eventually being overwhelmed by statistical error as t'/τ_η and $\mathrm{var}(w')$ reach very large values.

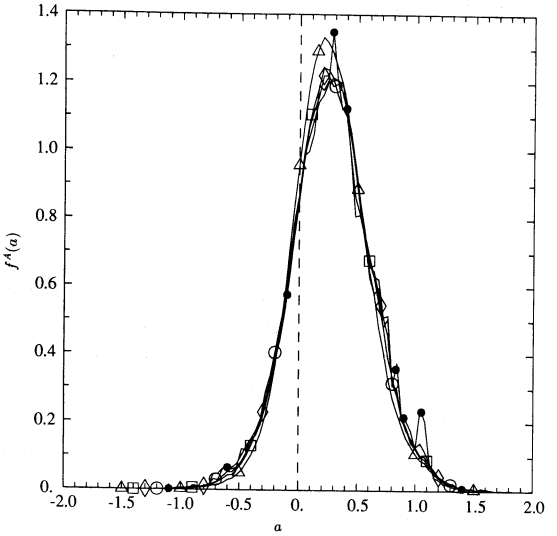

Fig. 21. Effect of time-lapse t' on area-weighting of the pdf of surface strain a, as illustrated by the R_λ 93 case using various values of t'/τ_η: △, 2.9; □, 7.0; ○, 11.1; ◇, 15.2; ●, 19.3. (The value $t' = 7.0\tau_\eta$ yields the area-weighted pdf shown in Fig. 6.)

Figure 20 shows the weighted variances of a and $\ln \chi_0$, for t' up to $20\tau_\eta$, calculated from the time series of a 64^3 simulation at R_λ 54 (see Ref. 23). In all the simulations studied so far in this article, averages are taken over 4096 fluid particles. However, in this case a smaller sample of 1600 fluid particles is used, thus providing a more severe test of statistical errors. As t' increases from zero, the variances are seen to approach their true area-weighted values, which are maintained over an appreciable interval of t'. The value of t' at the beginning of this interval can be considered to be t_s. For very large t', the surface strain variance is greatly affected by statistical error.

As expected from above, the acceptable range of t' increases with the time scale of the surface property considered. For the data of Fig. 20, we note that the integral time scales of a and χ_0 are about τ_η and $4\tau_\eta$ respectively. Guided by this and similar plots, we choose $t' \approx 7\tau_\eta$ and $t' \approx 11\tau_\eta$, respectively, for a and χ_0 (and same for $\ln \chi_0$). Satisfactory values for δ and z (in the stationary case) are found to be $11\tau_\eta$ and $15\tau_\eta$, respectively.

Figure 21 illustrates the effects of statistical errors on the area-weighted pdf of the surface strain a at R_λ 93, for several values of t'/τ_η. It may be seen that the $t' \approx 3\tau_\eta$ curve is separated from the others, indicating that it is not the true area-average. At $t' \approx 19\tau_\eta$, statistical errors are prominent, resulting in a spiky pdf (in the absence of curve-smoothing). This is in spite of the number of samples being 1.6×10^6, which is large compared to the number of bins (100) used in forming the histogram in the estimation of the pdf.[6]

The area-weighting strategy described above has been applied throughout the paper. Except in Fig. 21, area-weighted pdfs presented have been smoothed slightly where necessary.

[6] All pdfs in this article are estimated with 100 bins for each variable.